remote sensing

MDPI

Article

Land Use/Land Cover Mapping Based on GEE for the Monitoring of Changes in Ecosystem Types in the Upper Yellow River Basin over the Tibetan Plateau

Senyao Feng [1], Wenlong Li [1,*], Jing Xu [2], Tiangang Liang [1], Xuanlong Ma [3,4], Wenying Wang [5] and Hongyan Yu [6]

[1] State Key Laboratory of Herbage Improvement and Grassland Agro-Ecosystems, College of Pastoral Agriculture Science and Technology, Lanzhou University, Lanzhou 730000, China
[2] School of Agriculture and Forestry Economic and Management, Lanzhou University of Finance and Economics, Lanzhou 730020, China
[3] College of Earth and Environmental Sciences, Lanzhou University, Lanzhou 730020, China
[4] Institute of Yellow River Basin Green Development, Lanzhou University, Lanzhou 730020, China
[5] Department of Life Sciences, Qinghai Normal University, Xining 810008, China
[6] Service Guarantee Center of Qilian Mountain National Park in Qinghai, Xining 810008, China
* Correspondence: wllee@lzu.edu.cn; Tel.: +86-136-5945-1811

Abstract: The upper Yellow River basin over the Tibetan Plateau (TP) is an important ecological barrier in northwestern China. Effective LULC products that enable the monitoring of changes in regional ecosystem types are of great importance for their environmental protection and macro-control. Here, we combined an 18-class LULC classification scheme based on ecosystem types with Sentinel-2 imagery, the Google Earth Engine (GEE) platform, and the random forest method to present new LULC products with a spatial resolution of 10 m in 2018 and 2020 for the upper Yellow River Basin over the TP and conducted monitoring of changes in ecosystem types. The results indicated that: (1) In 2018 and 2020, the overall accuracy (OA) of LULC maps ranged between 87.45% and 93.02%. (2) Grassland was the main LULC first-degree class in the research area, followed by wetland and water bodies and barren land. For the LULC second-degree class, the main LULC was grassland, followed by broadleaf shrub and marsh. (3) In the first-degree class of changes in ecosystem types, the largest area of progressive succession (positive) was grassland–shrubland (451.13 km^2), whereas the largest area of retrogressive succession (negative) was grassland–barren (395.91 km^2). In the second-degree class, the largest areas of progressive succession (positive) were grassland–broadleaf shrub (344.68 km^2) and desert land–grassland (302.02 km^2), whereas the largest areas of retrogressive succession (negative) were broadleaf shrubland–grassland (309.08 km^2) and grassland–bare rock (193.89 km^2). The northern and southwestern parts of the study area showed a trend towards positive succession, whereas the south-central Huangnan, northeastern Gannan, and central Aba Prefectures showed signs of retrogressive succession in their changes in ecosystem types. The purpose of this study was to provide basis data for basin-scale ecosystem monitoring and analysis with more detailed categories and reliable accuracy.

Keywords: Google Earth Engine; land use/land cover mapping; machine learning; upper Yellow River basin; Sentinel-2; ecosystem types

Citation: Feng, S.; Li, W.; Xu, J.; Liang, T.; Ma, X.; Wang, W.; Yu, H. Land Use/Land Cover Mapping Based on GEE for the Monitoring of Changes in Ecosystem Types in the Upper Yellow River Basin over the Tibetan Plateau. *Remote Sens.* **2022**, *14*, 5361. https://doi.org/10.3390/rs14215361

Academic Editors: Yaqian He, Fang Fang and Christopher Ramezan

Received: 12 September 2022
Accepted: 22 October 2022
Published: 26 October 2022

1. Introduction

Land use/land cover (LULC) provides valid information for demonstrating the complex and continuous interactions between global-to-local ecosystem change and human behavior [1], and it can reveal the main drivers and consequences of global environmental change [2–4]. It is worth noting that although different regions may have radically different LULC expressions [5], their similar processes of change are constantly altering the energy

and material cycles at the Earth's surface [5], including the carbon [6], nitrogen [7], and water cycles [8–10]. With the increases in human-led LULC behavior in different parts of the world, such as agricultural expansion [11,12], urban expansion [13], and engineering projects [14], the ecosystem's structure and function [15], biodiversity [16–18], and services [19] are further disturbed, either positively or negatively [20–22]. This creates great uncertainty for regional ecosystems and ecological environments, and this will continue to increase, especially with global climate change [23]. In this context, achieving accurate LULC products at different spatial scales (local, national, and global) is essential for the regular monitoring of existing ecosystems [20], planning and management of natural resources [24], research and assessment of environmental quality [25], and promotion of sustainable regional development [24].

Early LULC product mapping was mainly based on field surveys and manual visual interpretation. This method is inefficient and costly, making it difficult to meet the need for the regular and timely monitoring and mapping of LULC [26]. With the rapid development of remote sensing (RS) technology, the development of LULC products at various temporal and geographical scales has become possible [27]. In the process, satellite data have improved dramatically in four directions: spatial [28,29] and temporal resolution [30], radiation, and spectra [31].For instance, Sentinel-2 has provided unprecedented free images with a spatial resolution of 10 m and a temporal resolution of 5 days to the world since 2015. Meanwhile, with the development of classification methods, machine learning algorithms (e.g., random forest (RF), gradient boosting decision tree (GBDT), and support vector machine (SVM)) have been widely used in the field of LULC mapping [32–35]. These have opened up new possibilities for more detailed LULC mapping [36]. However, they also pose tremendous challenges for the efficiency of RS data collection and processing [37]. To meet these challenges, Google Earth Engine (GEE), a big-data cloud-based network computing resource platform, has emerged, and it has demonstrated strong competitiveness in recent years. It provides massive geospatial datasets with unprecedented online computational and visual analysis capabilities [38,39]. Researchers could use the GEE platform [39] to pre-process or download multi-temporal image data that meet filtering requirements and then use various machine learning algorithms to perform LULC classification and analysis online. As a result, the GEE platform is increasingly being utilized to generate efficient and large-scale LULC products as well as change-monitoring studies [40].

The upper Yellow River basin over the Tibetan Plateau (TP), with a rich variety of ecosystem types, is an important ecological barrier [41] and corridor [42] in the northwest of China and TP. On the one hand, it is important an water supply and connotation area for the entire Yellow River basin and even the interior of northern China [43]. It plays a significant role in soil and water conservation, carbon sequestration, and animal husbandry, in addition to providing water for almost 20% of China's cropland and around 190 million people in the basin [44]. On the other hand, it is one of the most sensitive regions to global climate change [45], with an extremely fragile ecological environment [46]. During recent decades, its LULC and ecosystems have been dramatically altered by both human activities and climate change [47], so there is an urgent need for more detailed and regionally applicable LULC products to monitor and reveal the characteristics (positive or negative) of these changes. Some relevant LULC products are now obtainable for this region, such as FROM-GLC10, the world's first LULC product with a spatial resolution of 10 m based on Sentinel-2 imagery [48], FROM-GLC30 [1], and GlobeLand30 [24], with a spatial resolution of 30 m based on Landsat imagery. However, these existing products have entirely different classification schemes, data sources, methods, and spatial and temporal resolutions, and this has led to significant uncertainty in the classification details they provide. Furthermore, compared to other regions, the study area has more prominent high-altitude landscape heterogeneity, more complex landforms, and richer vegetation communities and ecosystem types, and, as a result, existing products are unable to fully distinguish and describe the LULC variations at the level of ecosystem types in the region. Therefore, it is necessary to take more detailed ecosystem types into account, to develop a

new classification scheme, and to produce high-resolution multi-category LULC products for the region to facilitate monitoring at the level of regional ecosystem types.

The study defined a two-level LULC classification scheme based on ecosystem types for the study area and produced LULC maps at 10 m spatial resolution based on the GEE platform, Sentinel-2 image data, and machine learning methods. The main objectives are as follows: (1) to generate products and assess their accuracies and performances; (2) to conduct monitoring of changes in ecosystem types based on LULC products. The results are helpful for the further mapping of LULC products over the whole Yellow River basin and provide new, effective data support for monitoring changes in basin-scale ecosystem types and ecological quality assessment.

2. Materials and Methods

2.1. Study Area

The upper Yellow River basin over TP (32°8′–38°20′N, 95°50′–104°31′E) is located in the westernmost part of the Yellow River basin in northwestern China. It lies on the western edge of the Loess Plateau and the northeastern part of the TP, spanning the Qinghai, Gansu, and Sichuan Provinces (Figure 1). The Yellow River originates here and flows through nine provinces or autonomous regions (Qinghai, Gansu, Sichuan, Ningxia, Inner Mongolia, Shaanxi, Shanxi, Henan, and Shandong) for 5464 km [49] (Figure 1b). The study area is approximately 1.99×10^5 km^2, accounting for about 26.5% of the entire Yellow River basin. It has a complex and diverse landscape, with many high mountains, canyons, basins, and hills sloping from the southwest to the northeast at altitudes of 1650–6254 m [42]. In addition, the study area straddles the plateau's temperate, semi-arid, and subfrigid semi-humid and humid zones and has a typical plateau continental climate, with long sunshine hours, strong solar radiation, long winters, and short summers. It also has an average annual temperature of −4–6 °C, which gradually decreases with increasing altitude, and an average annual precipitation of approximately 420–800 mm [41,43,50,51]. The complex landscapes and climatic types have given rise to a rich variety of LULC types in the study area [52], including mainly grassland, forest, agricultural land, barren land, and wetlands and water bodies (Figure 1d–h), which also makes it an important area for safeguarding ecosystem services in the Yellow River basin. The dynamics of its ecosystem types are closely related to the sustainable development of local socioeconomic development and environment protection.

2.2. Dataset

2.2.1. Satellite Data

In this study, Sentinel-2 multispectral imagery (MSI) from the vegetation growing season (image time range of 1 June to 30 August in 2018 and 2020) was used for composition and classification. Considering the shortage of 2018 Sentinel-2 SR images covering the study area in GEE, the downloading and processing of Sentinel-2 data was divided into two separate parts for 2018 and 2020.

At the ESA Copernicus Open Access Centre (https://scihub.copernicus.eu/dhus/, accessed on 21 March 2022), due to the unique geographical conditions and the phenomenon of high cloud cover in the study area, the threshold for cloud volume was set at 35%. In this context, 92 Sentinel-2A/B Level-1C (L1C) top-of-atmosphere (TOA) reflectance data with <35% cloud cover from the 2018 vegetation growing season were acquired, then batch processed to Level-2A (L2A) surface reflectance data using the radiative transfer model-based Sen2cor tool [53]. All bands were resampled to 10 m by the bilinear method and de-clouded by masking the clouds with a quality scene classification band provided by the L2A images [54]. After median compositing, mosaicking, and cropping the images, the cloud-free Sentinel-2 images from 2018 were finally uploaded to the GEE platform for classification [55].

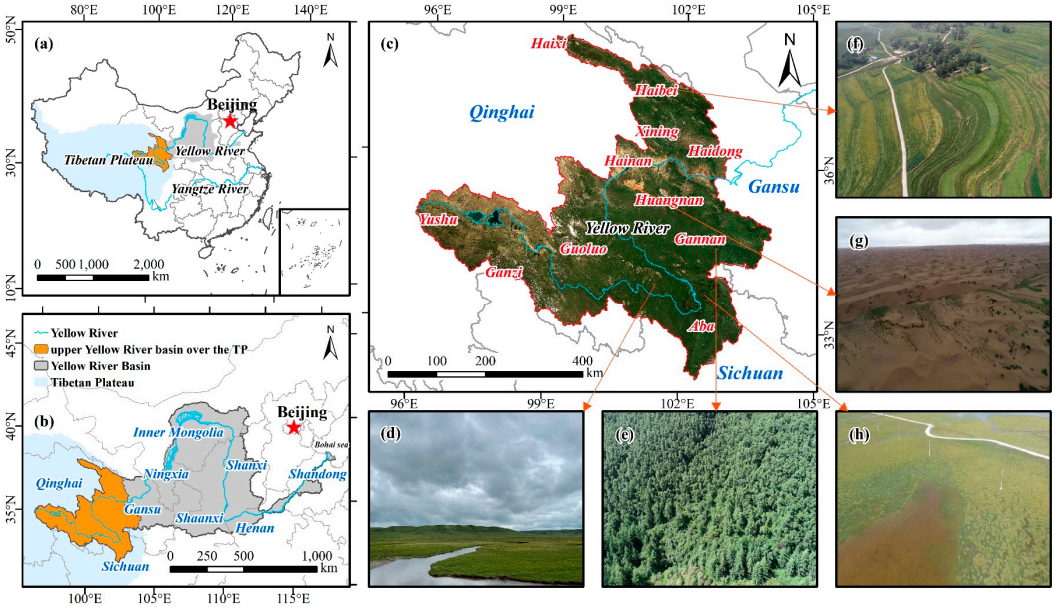

Figure 1. Location of the study area. (**a**) Location of the Yellow River basin in China; (**b**) location of the study area within the Yellow River basin and the Tibetan Plateau; (**c**) examples of true-color images and land use/land cover types for Sentinel-2 from June to August 2020 ((**d**): grassland, (**e**): forest, (**f**): agricultural land, (**g**): barren land, (**h**): wetland and water body).

Sentinel-2 data for 2020 were obtained online through the GEE platform (https://code.earthengine.google.com/, accessed on 6 April 2022). Sentinel-2 L2A images with <35% cloud cover in the study area during the vegetation growing season were retrieved (661 images in total), the cloud was masked through the quality assessment band (QA60) provided by the L2A images, and the subsequent image pre-processing, including resampling, median compositing, mosaicking, and cropping were completed through the GEE platform. Finally, cloud-free Sentinel-2 images from 2020 were obtained [56].

2.2.2. Terrain Data

The Shuttle Radar Topography Mission (SRTM) digital elevation model is available in the GEE platform database [57] with a spatial resolution of 30 m. In this study, the elevation, aspect, hill shade, and slope of the SRTM data were extracted as features for LULC classification using the GEE platform.

2.2.3. Land Use/Land Cover Dataset

The 10 m global-scale land use/land cover dataset FROM-GLC10 provided by Tsinghua University (http://data.ess.tsinghua.edu.cn/, accessed on 25 March 2022) [48], which was generated from Sentinel-2 imagery (spatial resolution of 10 m) from 2017, was used for comparison with the classification results of this study.

2.2.4. Sample Point Data

The field surveys and the collection of field sample points for various LULC types in the study area were conducted between July and August in 2018 and 2020 (Figure 2). Observations were made in areas that were accessible by vehicle, and the Trimble Juno series handheld GPS (https://www.trimble.com, accessed on 10 August 2020) was used to acquire and record information on the type and location of LULCs. Aerial photographs of different land cover types by DJI Phantom 4 and Mavic Pro light unmanned aerial vehicles (UAVs) [58] were used as accurate and reliable field interpretation signs. In 2018 and 2020, we collected a total of 8231 field survey points covering all LULC types in the study area (for 18 second-degree classes). The number of sample points in each class was adjusted with reference to the proportion of land cover area and the actual situation, eliminating

the impact of possible sample imbalance on the classification of a small number of rare LULC types [59]. In this case, the effect of sample unevenness on LULC classification was eliminated. In addition, for those remote areas that were difficult to reach by vehicle, such as the western end of the study area (Figure 2), we visually interpreted and collected 15,709 sample points using high-resolution Google Earth Pro and Sentinel-2 RGB true-color composite imagery. Finally, all sample points were checked individually against the high-resolution imagery provided by Google Earth Pro to confirm that the LULC categories for all sample points in 2018 and 2020 were consistent with the actual conditions [60]. In this process, 470 sample points were corrected and added. Then, 80% of the sample points were used as training samples for the classification, and 20% were used to verify the accuracy of the classification through a stratified random sampling method [61]. The set of training and validation points for the years 2018 and 2020 are shown in Table 1.

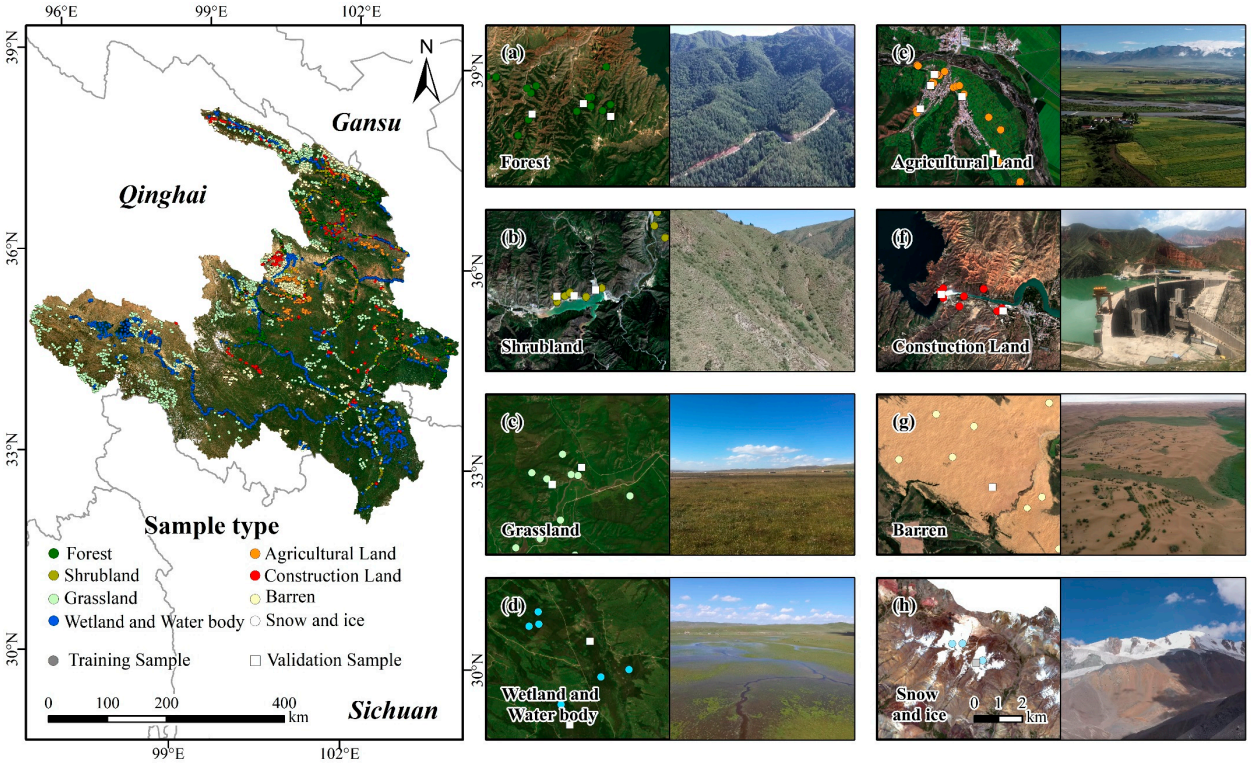

Figure 2. Spatial distribution of LULC first-degree class sample points. (**a**–**h**) Sentinel-2 RGB true-color composite image of LULC first-degree class sample points and aerial photographs of the field.

Table 1. Training and validation sample points in this study.

First-Degree Class	Second-Degree Class	2018		2020	
		Training Samples	Validation Samples	Training Samples	Validation Samples
Forest	Broadleaf Forest	332	83	320	80
	Needleleaf Forest	164	41	196	49
	Mixed Forest	408	102	384	96
Shrubland	Broadleaf Shrub	260	65	196	49
	Needleleaf Shrub	112	28	104	26
Grassland	Grassland	2908	727	2724	681

Table 1. *Cont.*

First-Degree Class	Second-Degree Class	2018		2020	
		Training Samples	Validation Samples	Training Samples	Validation Samples
Wetland and Water body	Marsh	412	103	448	112
	Lake	380	95	216	54
	River	1304	326	1432	358
Agricultural Land	Cropland	1268	317	1388	347
	Orchard Land	412	103	180	45
Construction Land	Urban	756	189	656	164
	Urban Green Space	92	23	120	30
	Industrial and Transportation Land	272	68	352	88
Barren	Desert Land	244	61	232	58
	Bare Soil	76	19	72	18
	Bare Rock	284	71	248	62
Snow and ice	Snow and ice	384	96	192	48
Total		10068	2517	9460	2365

2.3. Research Methods

The flow chart in Figure 3 shows the mapping and analysis methods applied in this study. Sentinel-2 image pre-processing, feature construction, sample selection, LULC classification, accuracy assessment, and the monitoring of changes in ecosystem types based on LULC are the main steps involved. The following sections describe the classification scheme and several relevant steps in this study in detail.

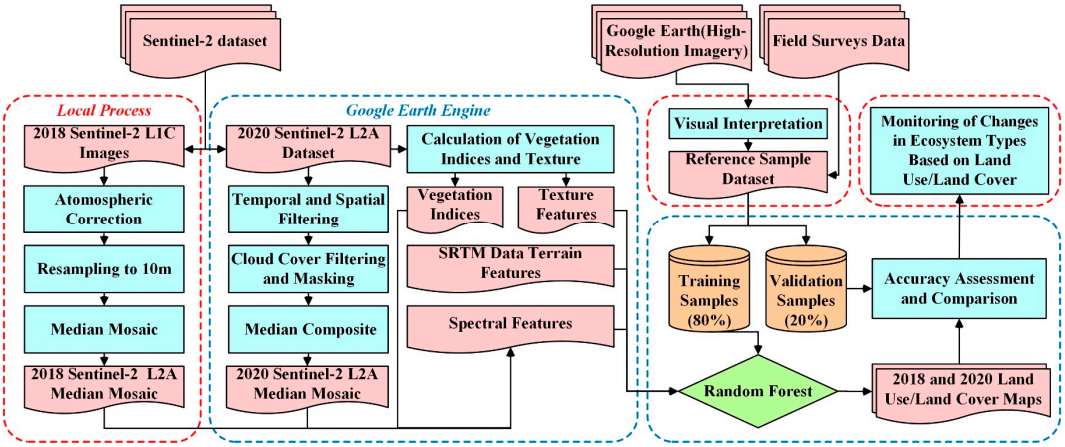

Figure 3. Flow chart of the land use/land cover (LULC) mapping and analysis methodology for this study.

2.3.1. Classification Scheme

Based on ecosystem types [62], taking into account the regional characteristics of the study area and the capability of the satellite data used and referring to the International Geosphere-Biosphere Programme (IGBP) classification system, existing land cover classification products covering it, and LULC classification research from other regions [42,62–65], a new two-level LULC classification scheme was defined (Table 2).

Table 2. The LULC classification scheme of this study.

First-Degree Class	Second-Degree Class	Description
Forest	Broadleaf Forest (BLF)	Dominated by broadleaf trees with a percent cover > 60% and height > 2 m.
	Needleleaf Forest (NLF)	Dominated by needleleaf trees with a percent cover > 60% and height > 2 m.
	Mixed Forest (MF)	Dominated by trees with cover > 60% and height > 2 m. Consists of tree communities with interspersed mixtures or mosaics of the other two forest types. Neither of the forest types exceeded 60%.
Shrubland	Broadleaf Shrub (BLS)	Dominated by broadleaf shrub with a percent cover > 60% and height < 2 m.
	Needleleaf Shrub (NLS)	Dominated by needleleaf shrub with a percent cover > 60% and height < 2 m.
Grassland	Grassland (Grass)	Dominated by herbaceous plants (<2 m) with a percent cover > 60% and height < 2 m.
Wetland and Water body	Marsh (Marsh)	Permanently inundated lands with wet-growing herbaceous or woody plants on the surface.
	Lake (Lake)	Natural, artificially constructed, relatively stationary water surface, including reservoirs, pits, fish ponds, salt ponds.
	River (River)	Naturally flowing linear water surface. Includes canals/channels: artificially constructed, flowing, linear water surfaces > 30 m wide.
Agricultural Land	Cropland (Crop)	Dominated by herbaceous annuals (temporary crops) (<2 m). At least 60% of area is cultivated cropland. Includes post-harvest bare soil period.
	Orchard Land (OL)	Lands with mainly a mosaic of commercial artificial forests or shrublands for cash crops.
Construction Land	Urban (Urban)	At least 60% of area is covered by residential building materials, such as cities, towns, and villages.
	Urban Green Space (UGS)	Artificially cultivated grassland in residential areas, including artificially cultivated recreational and sports grounds in the countryside.
	Industrial and Transportation Land (IAT)	At least 60% of the area is covered by industrial lands, transportation lands, and mining sites.
Barren	Desert Land (DL)	Lands with the ground completely covered by loose sand particles; never has > 10% vegetated cover during any time of the year.
	Bare Soil (BS)	Lands with the surface covered by exposed soil with loose structure; never has > 10% vegetated cover during any time of the year.
	Bare Rock (BR)	Lands with the surface covered by hard rock; gravel-covered surface; never has > 10% vegetated cover during any time of the year.
Snow and ice	Snow and ice (Snow)	At least 80% of the area is covered by snow/ice throughout the year.

Specifically, the ecosystem types of the study area are complex and diverse. On the premise that we were familiar with the basic characteristics of the different types of ecosystems, as well as the meaning of their attributes and their interpretative signs, we divided the LULC into eight primary classes (forest, shrub, grassland, wetland and water body, agricultural land, construction land, barren land, and snow and ice) based on the ecosystem types. On this basis, in order to be able to distinguish and monitor more details within the ecosystem types, the LULC classification scheme was increased to 18 second-degree classes.

For the purpose of LULC classification, we used the same training points for the first- (combining the training points of the second-degree classes into first-degree class for classification) and second-degree classes, then evaluated their accuracy with the same validation points. It is worth noting that to ensure the comparability of LULC area statistics and changes, we only used second-degree class training points to generate all LULC products for the study area (whereby primary first-degree classes were generated by second-degree class products) [60]. In addition, the spatial distribution of sample points for 18 secondary classes and sample selection examples for the Sentinel-2 RGB true color images are shown in Figure 4.

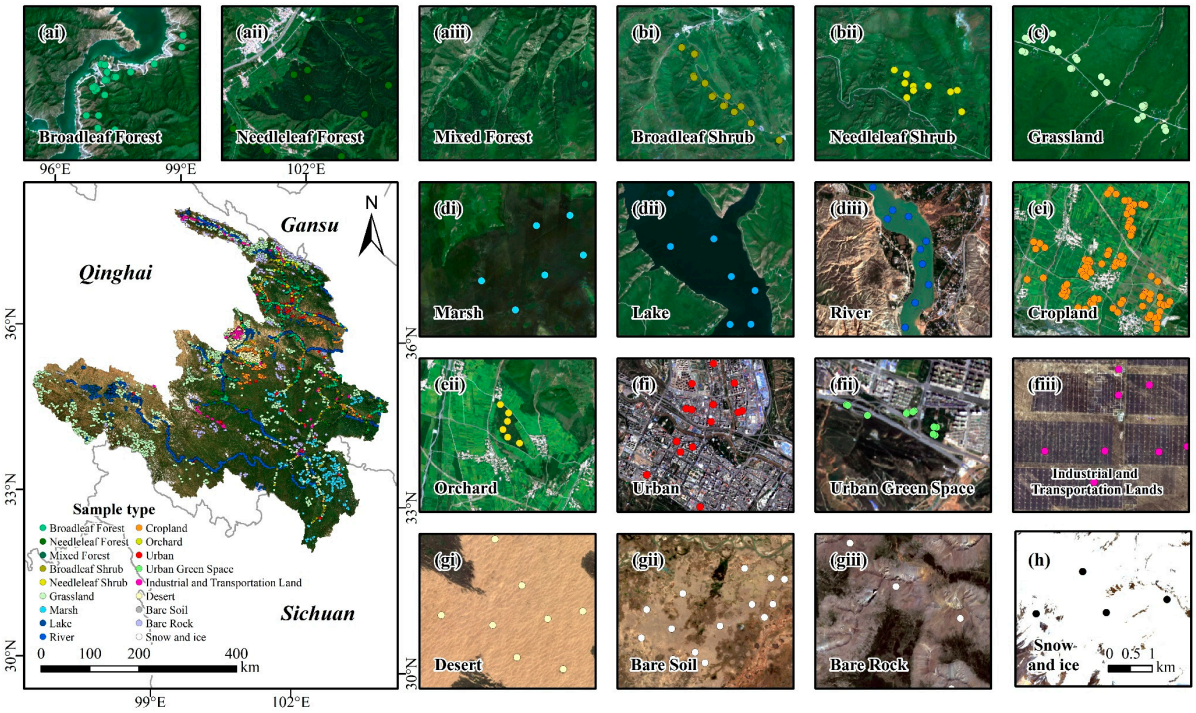

Figure 4. Spatial distribution of LULC second-degree class sample points. (**ai**–**h**) Sentinel-2 RGB true-color composite image of LULC second-degree class sample points.

2.3.2. Feature Construction

It is important to construct effective feature datasets to participate in LULC classification [66]. For the spectral features, first, based on previous studies and several tests [66–68], the Sentinel-2 L2A multispectral image bands that adequately conveyed the ecosystem types and LULC status of the study area were selected, including B2, B3, B4, B5, B7, B8, and B11. In addition, numerous studies have shown that different vegetation indices (VIs) as input features for classification will effectively improve the accuracy of LULC [26,69–71]. We used the GEE platform to calculate the NDVI (Normalized Difference Vegetation Index [72]), which characterizes the physiological, biochemical, and structural characteristics of the vegetation canopy; the NDWI (Normalized Difference Water Index [73]), which characterizes water bodies; the NDBI (Normalized Difference Building Index [74]), which characterizes manmade land surface features; the SAVI (Soil Adjusted Vegetation Index [75]), which highlights soil characteristics; and the EVI (Enhanced Vegetation Index [76]), which enhances the physiological, biochemical, and structural characteristics of the vegetation canopy. The formulas we used were as follows:

$$\mathrm{NDVI} = \frac{\mathrm{NIR} - \mathrm{Red}}{\mathrm{NIR} + \mathrm{Red}} \quad (1)$$

$$\mathrm{NDWI} = \frac{\mathrm{Green} - \mathrm{NIR}}{\mathrm{Green} + \mathrm{NIR}} \quad (2)$$

$$\text{NDBI} = \frac{\text{SWIR} - \text{NIR}}{\text{SWIR} + \text{NIR}} \quad (3)$$

$$\text{SAVI} = 1.6 \times \frac{\text{NIR} - \text{Red}}{\text{NIR} + \text{Red} + 0.6} \quad (4)$$

$$\text{EVI} = 2.5 \times \frac{\text{NIR} - \text{Red}}{\text{NIR} + 6 \times \text{Red} - 7.5 \times \text{Blue} + 1} \quad (5)$$

where NIR, SWIR, Red, Green, and Blue are the reflectance values from the near-infrared (842 nm), short-wave infrared (1610 nm), red (665 nm), green (560 nm), and blue (490 nm) bands of Sentinel-2, respectively.

Texture features are the patterns that result from a specific transformation of a gray-scale image in space. It has been shown that combining texture features with spectral information can improve the accuracy of LULC classification in specific scenarios [77,78]. For example, a recent study has combined GLCM texture features with spectral bands to classify forest tree species and achieved the highest OA (92%) [79], indicating that texture features are important for accurately distinguishing between LULC classes such as forest and shrubland. Currently, Grey-Level Co-occurrence Matrix (GLCM) computation has been widely used in the statistics and analysis of texture features [68,80,81]. As in previous studies [82], here, with the fast computation of the GLCM-based texture feature function *glcmTexture* provided by the GEE platform, and using a gray-level 8-bit image as input, the computation and construction of 18 texture features were completed. In this study, the Sentinel-2 images were first converted to gray-scale as input to the GLCM according to Equation (6), which involves operations between the red, green, and near-infrared bands of Sentinel-2:

$$\text{Gray} = (0.3 \times \text{NIR}) + (0.59 \times \text{RED}) + (0.11 \times \text{GREEN}) \quad (6)$$

where NIR, Red, and Green are the reflectance values from the near-infrared (842 nm), red (665 nm), and green (560 nm) bands of Sentinel-2, respectively.

Based on previous studies, we tested the neighborhood of 1, 2, 3, 5, 7, 10, 15, and 30 pixels, respectively, and finally set the GLCM's moving window to 5 × 5 pixels. Compared to other field settings, 5 × 5 pixels provides better recognition of the pixel-level texture in our study area [83]. Then, seven GLCM features including the angular second moment, contrast, correlation, entropy, variance, inverse difference moment, and sum average were calculated.

Topographic features greatly influence the accuracy of LULC classification of forest, shrubland, and agricultural land [50], so we extracted SRTMGL1_003 data provided by the GEE platform [39], including the elevation, slope, slope direction, and mountain shading. These were involved in the construction of the classification features along with texture and spectral features (Table 3).

Table 3. The set of features in this study.

Feature Type	Feature Name
Spectral	B2, B3, B4, B5, B7, B8, B11, NDVI, NDBI, NDWI, SAVI, EVI
Texture	Gray_asm, Gray_contrast, Gray_corr, Gray_ent, Gray_var, Gray_idm, Gray_savg
Terrain	Elevation, Slope, Aspect, Hill shade

2.3.3. GEE-Based Random Forest Classification

The random forest (RF) classifier is a non-parametric integrated learning algorithm based on the composition of multiple independent individual decision trees [84]. During the classification process, the voting process of all trees will determine the final classification result. RF can handle high-dimensional and multicollinear data accurately and robustly [85] and is much less sensitive to overfitting and training data quality [86,87]. At

the same time, RF eliminates the need for tree pruning and is computationally fast and less burdensome [88].

These advantages make RF competent for complex remote sensing image classification, and RF is therefore widely used in large-scale, multi-category, and multi-feature LULC mapping [89–91]. This study used a large study area (approximately 200,000 km^2) and large numbers of LULC classes (18 classes in total) and sample points (24,410 samples in total). Following the previous work in [22], the RF classifier set to 500 trees (ntree = 500) was able to be used for LULC classification work after several GEE user computation quota limit tests [86,89]; therefore, this study adopted RF as the classifier for LULC classification. In addition, the importance ranking function based on out-of-bag data error (OOBe) embedded in the RF classifier measures the contribution of individual features to the classification [84,86,92]. During the classification process, the importance scores of all the feature variables involved in the classification using the GEE platform were obtained and plotted [93].

2.3.4. Accuracy Assessment

A random sample of 20% of the sample point data for each of the years 2018 and 2020 was used for the LULC accuracy assessment. This validation set was completely independent of the training dataset and ensured a random distribution of validation points within the study area, with validation points available in each of the 18 second-degree classes.

The confusion matrix is a popular LULC accuracy evaluation method [94,95]. In this study, confusion matrices were constructed in GEE to evaluate LULC classification accuracy, and they then calculated the quantitative metrics' overall accuracy (OA), producer's accuracy (PA), user's accuracy (UA), and Kappa coefficient [96–98]. These indicators reflect the agreement between the LULC classification results and the actual LULC at the sites from different perspectives [99]. Four identical areas were selected for visual evaluation with existing LULC products to compare the differences in the spatial distribution of the classification results [91,100].

2.3.5. The Monitoring of Changes in Ecosystem Types

In this study, the monitoring of changes in ecosystem types was based on the LULC transition matrix and ecological succession theory.

An ecosystem is a comprehensive biological system consisting of all the organisms found and interacting with each other in a particular physical environment [101,102]. It includes multiple types such as the forest ecosystem, shrubland ecosystem, grassland ecosystem, freshwater ecosystem, and wetland ecosystem, among others. Ecosystems are not exactly equivalent to LULC, but the LULC can provide spatially continuous data for monitoring ecosystem change [103], whereby LULC transitions can reflect the change in ecosystem types [104]. Ecological succession is defined as the orderly process of reassembling vegetation communities or ecosystems following natural or anthropogenic disturbance [105,106]. It can also reflect changes in ecosystem types, including the progressive succession of ecosystem types, for example, the natural growth of grass from abandoned mines or bare soil [107], the artificial restoration of forests [108], and the retrogressive succession of ecosystem types [109], e.g., deforestation by humans or grassland desertification. In addition, some previous studies have shown that LULC transitions can reflect the occurrence of ecological succession [110–112], so it is reasonable to monitor changes in ecosystem types based on ecological succession theory combined with the LULC transition matrix.

For this study, ecological succession relationships between barren land, grassland, freshwater (river and lake), wetland (marsh), shrubland, and forest ecosystem types (including their second-degree classes) were considered. When change in ecosystem types was in the direction of progressive succession (positive), the transfer form was barren/freshwater–grassland/wetland–shrubland–forest, and, conversely, when the change in ecosystem types was in the direction of retrogressive succession (negative), the transfer form was

forest–shrubland–grassland/wetland–barren/freshwater. These change relationships are illustrated in Figure 5 and Table S1.

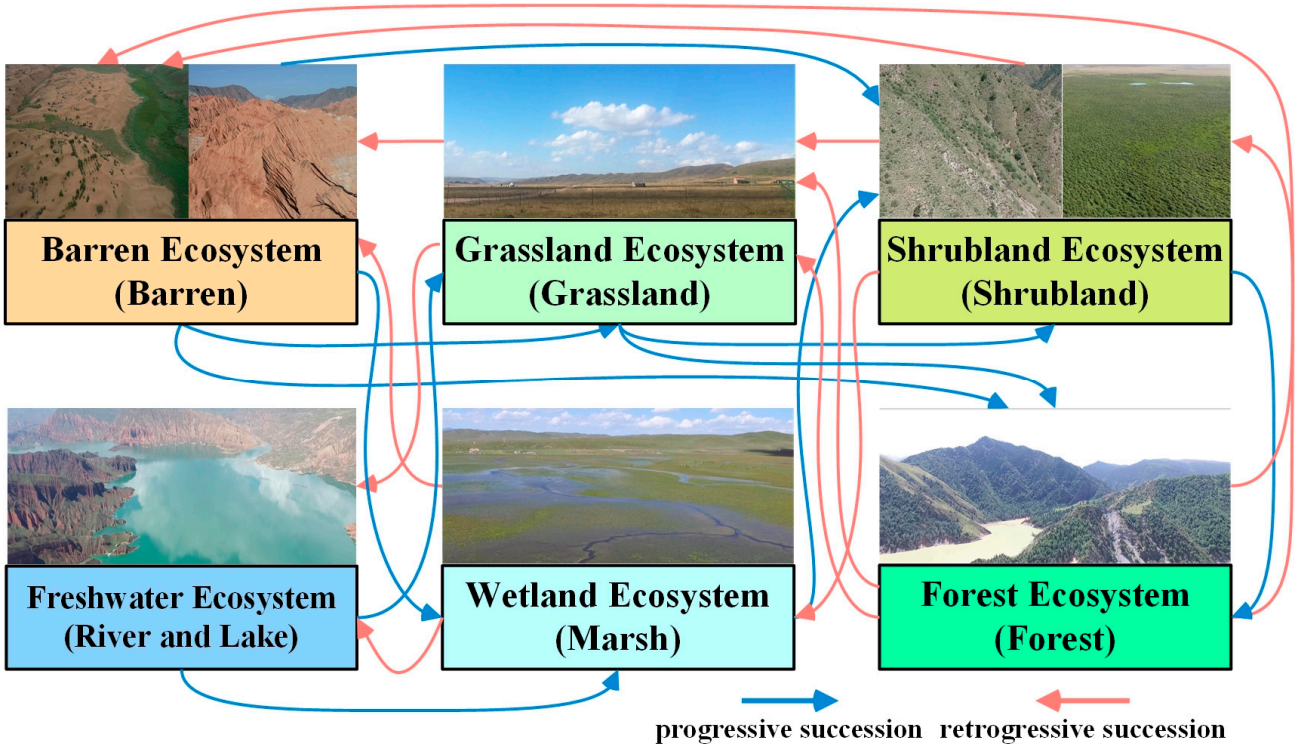

Figure 5. Schematic diagram of the ecological successions related to changes in ecosystem types. The LULC types under each ecosystem type are represented in parentheses.

3. Results

3.1. Feature Importance

Based on the feature importance ranking function, the average importance scores of the 23 feature variables involved in the LULC classification in 2018 and 2020 were plotted (Figure 6). The importance of the spectral features was typically high in all cases; the textural features were low, and, among the topographic features, the elevation (average 2095.82) and slope (average 2100.91) were high, whereas hill shade and aspect were low. Specifically, the B11, B2, B3, and B5 bands of Sentinel-2 were generally high in importance over the two-year period (mean > 1900), with B11 being the most important (average 2228.14). NDBI received the highest importance score (average 2059.84) of the five VIs, and NDWI was also ranked highly (average 1907.12). Of the texture features, Gray_savg had the highest importance (average 1858.31), and several others had the lowest importance (all < 1600). It is noteworthy that although only one of the texture features performed better, we found that the accuracy of LULC decreased when texture features were not included for classification (Table S2); this has been reported in a previous work [60]. Overall, B11, elevation, slope, B2, and NDBI were the most important features, whereas Gray_ent, Gray_asm, hill shade, and aspect contributed less to the LULC classification.

3.2. LULC Accuracy Assessment

The confusion matrix (Tables 4, 5, and S3–S6) showed good classification results for the LULC products generated in both 2018 and 2020. The OA of the first-degree class reached 90.58% and 93.02%, with Kappa coefficients of 0.88 and 0.91, respectively, and the OA of the second-degree class reached 87.45% and 92.14%, with Kappa coefficients of 0.85 and 0.91, respectively. Figure 6 shows that in terms of PA and UA, good accuracies (75.00% to 97.88%) were achieved for most of the LULC first-degree class, such as wetland

and water body, barren land, grassland, agricultural land, and forest. For both the 2018 and 2020 class I categories, water performed best in both PA (95.99% and 97.67%) and UA (97.33% and 97.88%), probably due to the better applicability of NDWI for identifying wetland and the more pronounced spectral response of water bodies compared to other LULC types [100]; the accuracies for shrubland were generally lower, and there were some misclassifications with forests and grasslands (Figure 7a,c and Tables S3 and S4). The addition of more subclasses led to an overall decreasing trend in the classification performance of the LULC second-degree classes, especially for the orchard and urban green space (Tables S5 and S6); these two showed more mixed and misclassified scores, with both PA and UA fluctuating around 80%. There were some misclassifications between urban land, cropland, and orchard, as all of these are classes that are relatively heavily influenced by human activities [42] (Table S5). Further, there was a small amount of misclassification between cropland, urban land, and grassland (Tables S5 and S6) due to the similar spectral characteristics between degraded grassland and post-harvest cropland and urban land. In contrast, broadleaf, needleleaf, and mixed forest showed good classification performance, with PA and UA generally above 80%. Of all the second-degree classes, the river, lake, marsh, farmland, grassland, bare rock, and snow were the best classified, with both PA and UA above 83% (Figure 7b,d and Tables S5 and S6). Considering the large number of LULC types involved in this work, it achieved more satisfactory results for all indicators of accuracy assessment.

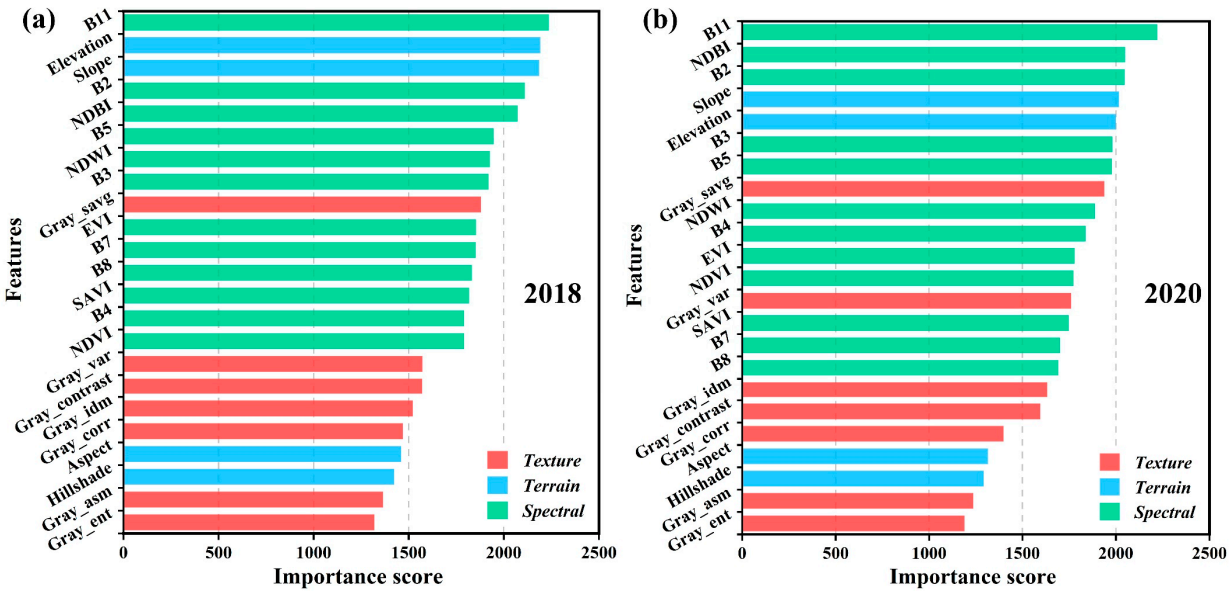

Figure 6. Average importance of features. (**a**) 2018; (**b**) 2020.

3.3. LULC Visual Assessment

For a more comprehensive assessment of LULC results, Figure 8 shows the high-resolution image provided by Google Earth Pro, the Sentinel-2 true-color image, the FROM-GLC10 product, and our LULC map, respectively. Four areas covering multiple LULC types for comparison were selected. It was found that our LULC results had a high fit with the field conditions of the high-resolution and Sentinel-2 true-color images, and there were some differences to the FROM-GLC10 product. For example, the extraction of town, road, and river information in our LULC results was more complete compared to FROM-GLC10 (Figure 8a). In the identification of desert (Figure 8b) and marsh (Figure 8c), our spatial distribution was similar to FROM-GLC10, but we had relatively less noise and provided more LULC detail, especially in the more accurate spatial distribution of marsh that we produced. However, although we did better in extracting the types of marsh, urban land,

cropland, and roads, there was still some localized mixing and misclassification of forest, shrubland, and grassland (Figure 8d).

Table 4. The confusion matrix of LULC first-degree class accuracy (PA: producer's accuracy; UA: user's accuracy; OA: overall accuracy).

LULC First-Degree Class	2018		2020	
	PA (%)	UA (%)	PA (%)	UA (%)
Forest	91.59	87.34	95.56	92.67
Shrubland	75.27	81.39	85.33	86.49
Grassland	92.02	90.53	92.66	92.66
Wetland and Water body	95.99	97.67	97.33	97.88
Agricultural Land	90.00	88.94	93.11	91.94
Construction Land	81.79	86.09	86.88	90.74
Barren	88.74	88.16	97.10	88.74
Snow and ice	93.75	92.78	75.00	92.31
OA (%)	90.58		93.02	
Kappa Coefficient	0.88		0.91	

Table 5. The confusion matrix of LULC second-degree class accuracy (PA: producer's accuracy; UA: user's accuracy; OA: overall accuracy).

LULC Second-Degree Class	2018		2020	
	PA (%)	UA (%)	PA (%)	UA (%)
Broadleaf Forest	89.16	80.43	90.00	83.72
Needleleaf Forest	80.49	80.49	89.80	91.67
Mixed Forest	79.41	81.00	87.50	91.30
Broadleaf Shrub	80.00	83.87	81.63	80.00
Needleleaf Shrub	89.29	89.29	80.77	87.50
Grassland	90.10	91.61	94.57	93.33
Marsh	90.29	94.90	90.18	87.07
Lake	86.32	94.25	94.44	94.44
River	93.25	87.61	97.49	98.59
Cropland	87.38	83.94	94.52	94.80
Orchard Land	72.82	75.00	82.22	80.43
Urban	80.95	88.44	88.41	90.63
Urban Green Space	82.61	86.36	76.67	76.67
Industrial and Transportation Land	85.29	81.69	85.23	87.21
Desert Land	96.72	81.94	91.38	94.64
Bare Soil	84.21	88.89	94.44	85.00
Bare Rock	87.32	96.88	87.10	87.10
Snow and ice	86.46	85.57	85.42	91.11
OA (%)	87.45		92.14	
Kappa Coefficient	0.85		0.91	

Furthermore, when comparing the proportion of the study area occupied by the different LULC types in our product with FROM-GLC10 (Figure S1), it was found that the proportions of grassland, construction land, agricultural land, snow, and ice were not much different from FROM-GLC10. However, there were obvious differences in the proportions of the forest, shrubland, wetland, and waterbody areas. Further visual assessment using the 2018 validation points of marsh, shrub, and forest and the UAV aerial photographs was conducted (Figure S2). In these areas, we found that our products performed relatively better for marsh (wetland), shrubland, and forest compared to FROM-GLC10 (Figure S2), which may be due to differences in the definitions of LULC types in different classification

systems and classification methods. Overall, the LULC products for the upper Yellow River basin over TP were reasonably consistent with the FROM-GLC10 products and have high accuracy, and they can be used in subsequent analysis.

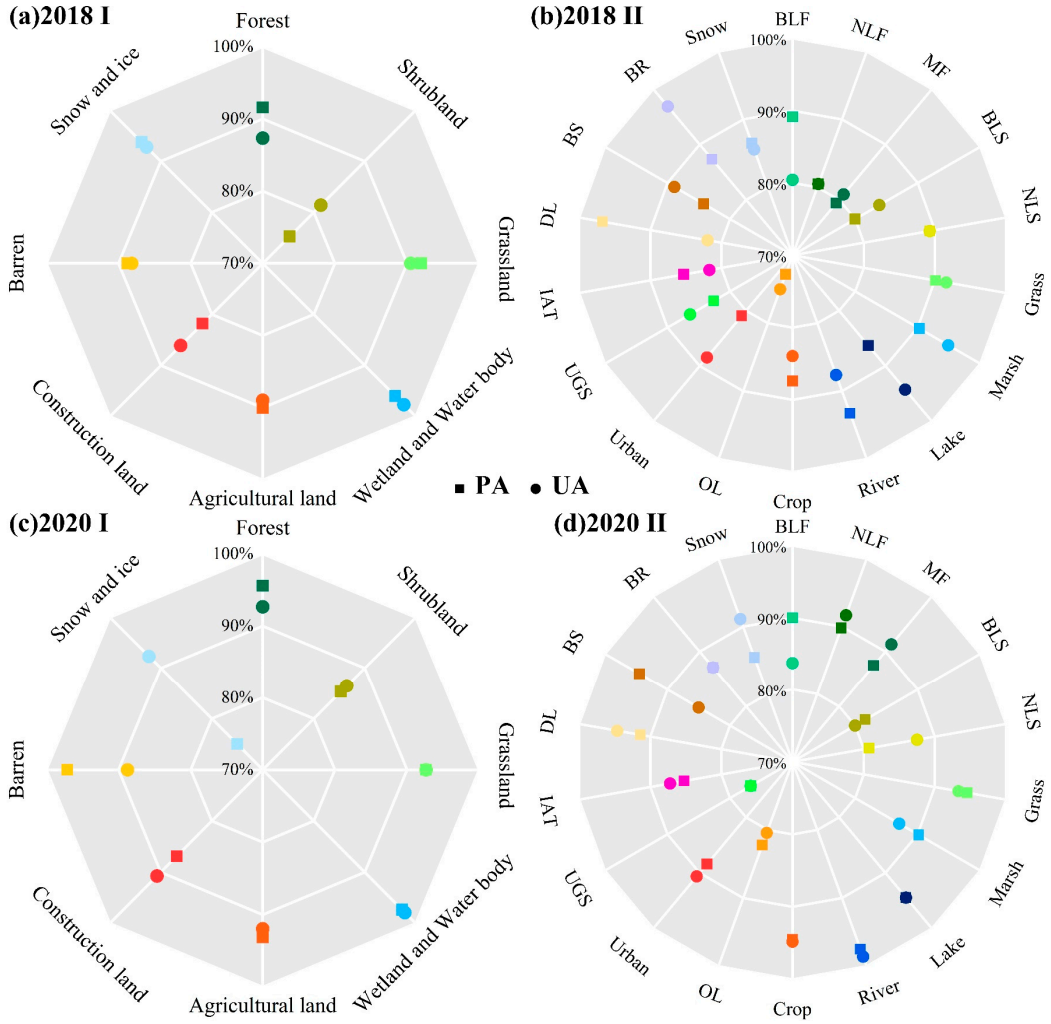

Figure 7. Producer's accuracy (PA) and user's accuracy (UA) for all LULC types: (**a**) first-degree class in 2018; (**b**) second-degree class 2018; (**c**) first-degree class 2020; (**d**) second-degree class 2018 in 2020.

3.4. LULC Classification Results

The results of the LULC classification and area statistics for the study area are shown in Figure 9 and Figure S3. In both 2018 and 2020, the most dominant LULC first-degree class in the study area was grassland (75.43% in 2018 and 75.44% in 2020), mainly in the western part of the Haibei, Hainan, Huangnan, Gannan, Guoluo, and Yushu Prefectures (Figure 8a,b). This was followed by the wetland and water body (6.09% in 2018, 5.89% in 2020), which was mainly concentrated in the western Guoluo, northern Hainan, southern Huangnan, southwestern Gannan and Aba Prefectures. Barren land (3.99% in 2018, 3.98% in 2020) was widely distributed at higher altitudes in the Yushu, Guoluo, central Hainan, and northern Haibei Prefectures. Shrubland (3.31% in 2018 and 3.22% in 2020) and agricultural land (3.13% in 2018 and 3.10% in 2020) were concentrated in areas with lower elevations, more abundant water resources, and suitable temperatures, such as Xining, Haidong, and the western Haibei and eastern Gannan Prefectures. In addition to grassland, the main LULC second-degree classes in the study area were broadleaf shrub (2.42% in 2018 and 2.31% in 2020), marsh (3.22% in 2018 and 3.07% in 2020), cropland (3.02% in 2018 and 2.99% in 2020), bare rock (2.78% in 2018 and 2020), and urban land (2018 1.51% and

1.66% in 2020); the urban areas were mainly located in the northern and central parts of the study area.

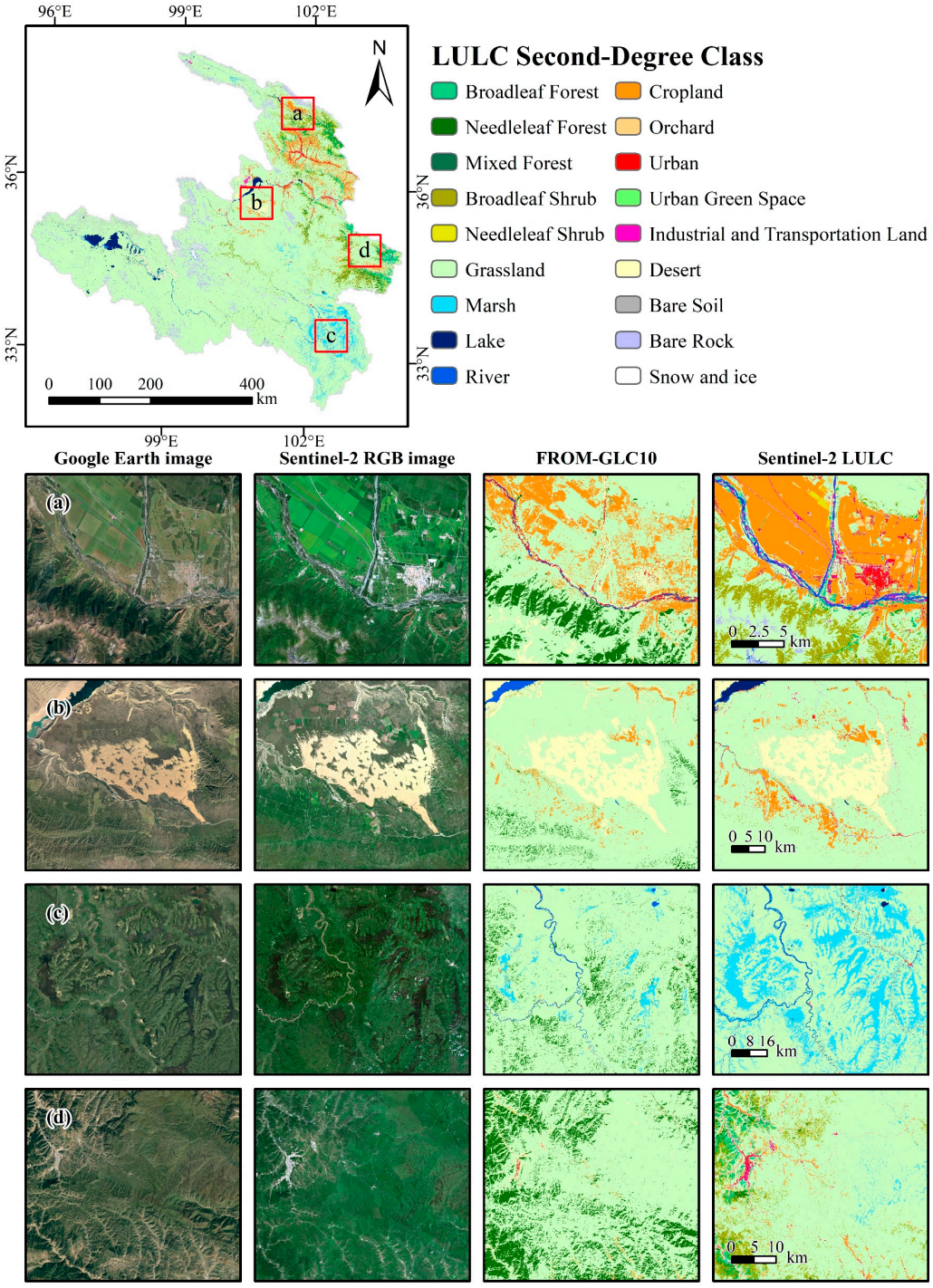

Figure 8. Visual comparison of this study with Google Earth, Sentinel-2 RGB, and FROM-GLC10 products. (**a**–**d**) Four typical areas were selected for close-ups.

3.5. Monitoring Changes in of Ecosystem Types Based on LULC Products

Based on the LULC transition matrices (Figure 10a,b) and ecological succession theory (Figure 5, Table S1), the changes in ecosystem types (Figure 10c,d) and their spatial distribution (Figure 10e) were obtained.

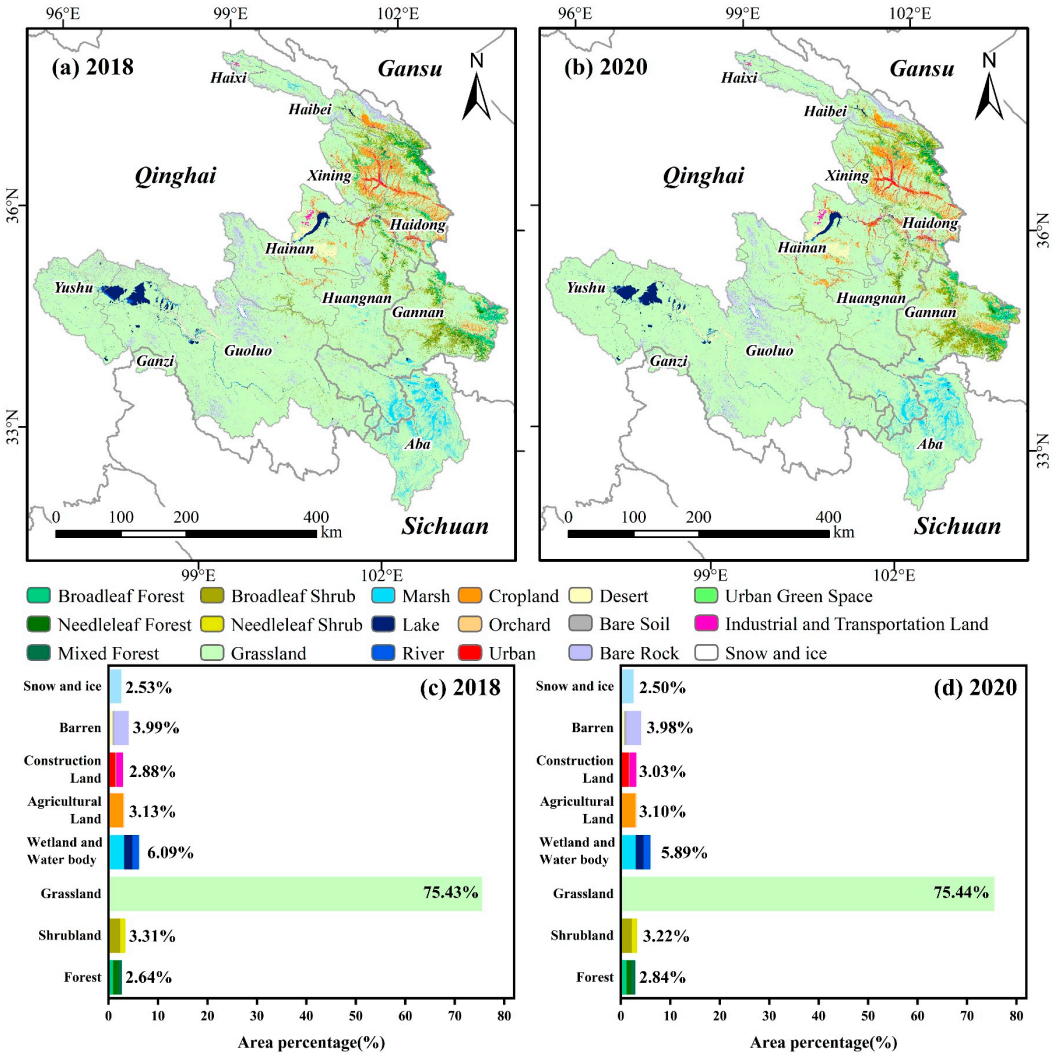

Figure 9. Spatial distribution of LULC second-degree classes in the study area in 2018 (**a**) and 2020 (**b**); area share of different LULC types in 2018 (**c**) and 2020 (**d**).

In the first-degree class of changes in ecosystem types (Figure 10c), the largest areas of progressive succession (positive) were grassland–shrubland, barren–grassland, and grassland–forest, with areas of 451.13 km^2, 425.93 km^2 and 405.95 km^2, respectively, whereas the smallest areas of progressive succession (positive) were freshwater–wetland, barren–wetland and freshwater–grassland, with areas of 34.75 km^2, 28.66 km^2, and 20.51 km^2, respectively. The largest areas of retrogressive succession (negative) were grassland–barren, shrubland–grassland, and shrubland–barren, with areas of 395.91 km^2, 326.84 km^2, and 240.38 km^2, respectively, whereas the smallest areas of retrogressive succession (negative) were wetland–barren, shrubland–wetland, and wetland–freshwater, with areas of 107.63 km^2, 68.13 km^2 and 39.94 km^2, respectively.

In the second-degree class of changes in ecosystem types (Figure 10d), the largest areas of progressive succession (positive) were grassland–broadleaf shrub, desert land–grassland, grassland–broadleaf forest, and desert land–broadleaf shrub, with areas of 344.68 km^2, 302.02 km^2, 267.91 km^2, and 144.75 km^2, respectively, whereas the smallest areas of progressive succession (positive) were river–grassland, desert land–mixed forest, desert land–marsh, and needleleaf shrub–broadleaf forest, with areas of 7.71 km^2, 9.11 km^2, 9.32 km^2, and 10.03 km^2, respectively. The largest areas of retrogressive succession (negative) were broadleaf shrub–grassland, grassland–bare rock, grassland–desert land, and broadleaf shrub–desert land, with areas of 309.08 km^2, 193.89 km^2, 191.16 km^2, and 77.04 km^2, respectively, whereas the smallest areas of retrogressive succession (nega-

tive) were needleleaf forest–bare soil, mixed forest–desert land, needleleaf forest–desert land, and broadleaf forest–needleleaf shrub, with areas of 3.55 km^2, 5.27 km^2, 6.30 km^2, and 10.57 km^2, respectively.

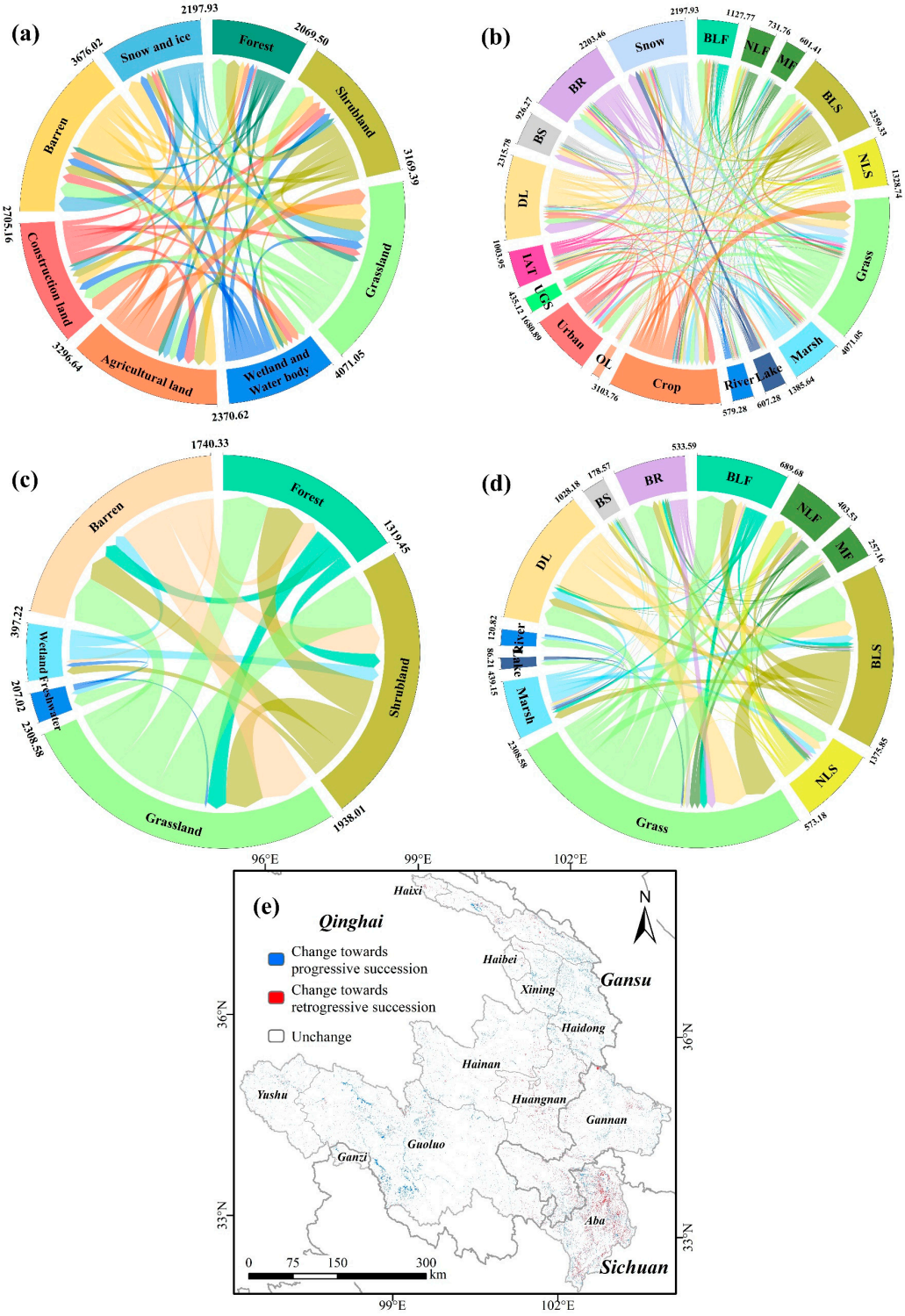

Figure 10. 2018–2020 LULC transition matrix and changes in ecosystem types; the width of the chord represents the area of the transfer. (**a**) First-degree class transition matrix chord diagram; (**b**) second-degree class transition matrix chord diagram; (**c**) first-degree class chord diagram of changes in ecosystem types; (**d**) second-degree class chord diagram of changes in ecosystem types; (**e**) distribution of changes in ecosystem types based on ecological succession and LULC.

The distribution of changes in ecosystem types based on LULC types for the source and the upper Yellow River basin from 2018 to 2020 was quantified and produced (Figure 10e). As can be seen from the figure, the changes in ecosystem types showed a trend towards positive succession (positive) in the northern and southwestern parts of the study area, whereas in the south-central Huangnan, northeastern Gannan, and central Aba Prefectures, it showed signs of retrogressive succession (negative) in ecosystem change.

4. Discussion

4.1. Comparison of Classification Methods

To further verify and assess the performance of the RF method for high-resolution LULC mapping in the study area, a comparison of the classification accuracy with three machine learning methods widely used in GEE were obtained, including classification and regression trees (CART), the gradient boosting decision tree (GBDT), and the support vector machine (SVM) (Table 6). The results showed that RF performed best among all the classifiers (87.45–92.14%), followed by GBDT [113] (86.65–90.60%) and CART [114] (78.76–86.99%), whereas the SVM [115] (74.64–84.30%) classifier had the lowest performance. The difference in effectiveness between the two integrated learning algorithms, GBDT and RF, was not significant, with RF slightly more effective than GBDT in this study; however, GBDT has shown better classification performance in some studies [116]. It is worth noting that although SVM performed far worse than RF and GBDT here, it has achieved good results in some classification studies [117–119], particularly those with relatively small training samples and LULC types [120], in which it can outperform RF. Although some studies have shown little difference in classification performance between SVM and RF [121,122], the classification performance of SVM is clearly limited when working with large-scale LULC mapping with a large number of training samples as in this study; RF and GBDT perform better in this respect.

Table 6. Comparison of the accuracy of several machine learning methods.

Machine Learning Methods	2018		2020	
	OA (%)	Kappa Coefficient	OA (%)	Kappa Coefficient
Random Forest	87.45	0.85	92.14	0.91
CART	78.76	0.75	86.99	0.85
Gradient Boosting Decision Tree	86.65	0.84	90.60	0.89
Support Vector Machine	74.64	0.70	84.30	0.81

4.2. Comparison of LULC Products Accuracy

In a visual comparison with the FROM-GLC10 product, our product provided more detail and had better performance in the extraction of cropland, urban land, rivers, and desert, but forest, shrubland, and grasslands showed some misclassification. In the first-degree class (Table 4), satisfactory accuracy (PA and UA > 80%) was achieved in almost all LULC types, except for shrubland (PA = 75.27%) and snow and ice. This result is similar to the GEE-based classification of the Qilian Mountains by Yang et al. [50]; the PA of the shrubland only reached 66.67% in their work. There was some visual similarity between both shrubland and degraded grassland and sparse forest, and that led to significant misclassification in transitional areas. The misclassification of snow and ice was mainly attributed to the persistence of clouds in the southern part of the study area that were hard to remove.

In the second-degree class, a large proportion of the LULC classes (15 out of 18) showed good accuracy (PA and UA > 80%), with reduced misclassification of shrubland and lower accuracy for the orchard (PA = 72.82%), urban green space, and mixed forest (Table 5). This result is similar to the LULC of the Yellow River basin by Ji et al. [42]; the PA of the orchard and terrace reached 0.74 in their work. The fact that orchard and urban

green spaces have relatively similar vegetation types in composition makes them extremely easy to confuse both spectrally and texturally [120]. Similarly, the only difference between mixed, needleleaf, and broadleaf forest classes is the ratio of needleleaf/broadleaf forest. The same problem affects the classification of second-degree classes such as construction land, shrubland, and barren land; in other words, even if we could accurately identify these secondary categories from field-collected UAV data or Google Earth Pro high-resolution imagery, there would still be a high degree of uncertainty in the classification, and it would still be challenging to capture these LULC types accurately [68]. Although we achieved a high degree of accuracy in our study, there are still some confusion problems in these secondary classes.

4.3. Changes in Ecosystem Types Based on Ecological Succession and LULC

Human activities and natural environmental changes, through their impact on LULC, largely influence the process of ecological succession and ultimately lead to the occurrence of changes in ecosystem types [112]. Traditionally, change in ecosystem types is relatively slow [123], especially for areas with low anthropogenic disturbance such as the upper Yellow River basin over TP; however, our study shows that approximately 3955 km^2 of the study area underwent changes in ecosystem types between 2018 and 2020. This implies that changes in ecosystem types are accelerating under the predominant role of anthropogenic disturbance.

The monitoring of changes in ecosystem types revealed both positive and negative effects of anthropogenic disturbances on ecosystem changes during this process. For the retrogressive succession, artificial disturbances often play a negative role: the change in ecosystem types of the grassland–desert land (191.16 km^2) may be associated with desertification of grasslands due to overgrazing; the change in ecosystem types of the broadleaf forest–grassland (70.49 km^2) is possibly associated with deforestation.

However, for the progressive succession, anthropogenic disturbances often play a positive role: the changes in ecosystem types of the grassland–broadleaf shrub (344.68 km^2) and desert land–broadleaf shrub (144.75 km^2) may be related to the local ecological barrier project in recent years; the change in ecosystem types of the desert land–grassland (302.02 km^2) confirms the overall increase in ecosystem services in the Sanjiangyuan area of the TP, as noted in recent reports [124], and that the ongoing efforts to combat desertification and related ecological restoration have been effective [47]. The change in ecosystem types of the grassland–broadleaf forest (267.91 km^2) may be related to a combination of ecological restoration projects such as reforestation and afforestation [22,47,125]. These findings illustrate the important role of LULC products that can be used for monitoring of regional ecosystem types and further confirm the reliability of our LULC products for monitoring of changes in ecosystem types.

4.4. Limitations and Prospects

Relying on the free GEE platform, we were able to carry out large-scale high-resolution LULC mapping work [36,38,126]. Unfortunately, Sentinel-2 cannot currently be used to monitor LULC changes over long time series. In addition, our research area is located at the eastern edge of the TP, where high altitudes and frequent variable weather rendered it permanently covered by clouds. Although multi-temporal compositing and cloud masking with GEE can compensate for this to some extent, monitoring still suffered in some areas, especially in the densely cloudy upper Yellow River basin [22,127]. Moreover, for the study area, GEE has not yet provided Sentinel-2 L2A(SR) data for 2018 and earlier; only L1C (TOA) data are available. Even though the relevant studies concluded that the effect of TOA data on classification is minimal [128], we still chose to use SR data for classification to better map the complex LULC distribution. This meant we spent more time on image pre-processing and reduced the efficiency of mapping LULC.

Despite these limitations, based on the processing framework and the new classification scheme of this study, one or more (2022, 2024, and so on) LULC maps that can be

used for monitoring of changes in ecosystem types will be easily obtained. At the same time, with the enrichment of classification algorithms' multi-source RS data and cloud computing platform, larger scale, higher resolution, and higher accuracy products can be provided when monitoring at the level of ecosystem types. In future research, we will generate more detailed high-resolution LULC products to promote regional ecological surveys and conservation.

5. Conclusions

The study combined an 18-class LULC classification scheme based on ecosystem types with Sentinel-2 multi-temporal data, the GEE platform, and the RF machine learning method to present new high-resolution LULC products with a spatial resolution of 10 m for the upper Yellow River basin over the TP and conducted monitoring of changes in ecosystem types. The main findings were as follows: (1) Combining Sentinel-2 imagery and RF classification methods, the products of the upper Yellow River basin over TP that were obtained based on the GEE platform have high classification accuracies and are suitable for monitoring changes in ecosystem types in the study area. (2) The LULC products based on a two-level classification system show that in the LULC first-degree class, the grassland, wetland and water body, barren land, shrubland, and agricultural land are the main LULC types. In the LULC second-degree class, grassland, broadleaf shrub, marsh, cropland, bare rock, and urban land are the main LULC types. (3) In 2018–2020, in the first-degree class of changes in ecosystem types, the largest areas of progressive succession (positive) were grassland–shrubland and barren–grassland, whereas the smallest areas were freshwater–wetland and barren–wetland. The largest areas of retrogressive succession (negative) were grassland–barren and shrubland–grassland, whereas the smallest areas were wetland–barren and shrubland–wetland. In the second-degree class of changes in ecosystem types, the largest areas of progressive succession (positive) were grassland–broadleaf and shrubland desert land–grassland, whereas the smallest areas of progressive succession were river–grass and desert land–mixed forest. The largest areas of retrogressive succession (negative) were broadleaf shrub–grassland and grassland–bare rock, whereas the smallest areas were needleleaf forest–bare soil and mixed forest–desert land. The northern and southwestern parts of the study area showed a trend towards positive succession, whereas the south-central Huangnan, northeastern Gannan, and central Aba Prefectures showed signs of retrogressive succession in changes in ecosystem types. This study can provide effective data support for the monitoring of regional scale ecosystem types, quality assessments and protection, natural resource management, and sustainable development of the upper Yellow River basin over the TP.

Supplementary Materials: The following supporting information can be downloaded at: https://www.mdpi.com/article/10.3390/rs14215361/s1, Figure S1: Ratios (%) of different LULC types areas between this study and FROM-GLC10; Figure S2: Visual comparison and assessment of this study with Sentinel-2 RGB, FROM-GLC10 products and UAV aerial photographs; Figure S3: Spatial distribution of LULC first-degree classes in the study area in 2018 and 2020; Figure S4: The map of changes in ecosystem types based on LULC types; Table S1: Relationships of changes in ecosystem types; Table S2: The accuracies with different feature combinations in 2018 and 2020; Table S3: Confusion matrix of LULC first-degree classes accuracy assessment in 2018; Table S4: Confusion matrix of LULC first-degree classes accuracy assessment in 2020; Table S5: Confusion matrix of LULC second-degree classes accuracy assessment in 2018; Table S6: Confusion matrix of LULC second-degree classes accuracy assessment in 2020; Table S7: Transition matrix of LULC first-degree classes in 2018-2020; Table S8: Transition matrix of LULC second-degree classes in 2018-2020; Table S9: Accuracy comparison (%) of the LULC classification result obtained in this study with the FROM-GLC10 (2017) land cover products in 2018.

Author Contributions: Conceptualization, W.L.; Formal analysis, S.F.; Funding acquisition, W.W. and H.Y.; Investigation, S.F.; Methodology, T.L.; Project administration, J.X.; Resources, X.M.; Supervision, T.L.; Validation, W.L.; Writing—original draft, S.F.; Writing—review and editing, S.F. and W.L. All authors have read and agreed to the published version of the manuscript.

Funding: This research was funded by the National Natural Science Foundation of China (grant No. 31170430, grant No. 41471450); the earmarked fund for the China Agriculture Research System (grant No. CARS-34); the Fundamental Research Funds for the Central Universities (grant No. lzujbky-2021-ct11); the funds for investigation and monitoring of typical forest, shrub, and meadow ecosystems in the vertical distribution zone of the Haibei region of the National Park (grant No. QHXH-2021-017); the Protection and Restoration of Muli Alpine Wetland in Tianjun County (grant No. QHTM-2021-003); the Key Entrusted Program of Lanzhou University of Finance and Economics (grant No. Lzufe2021W-003); and the Science and Technology Program of Gansu Province, China (grant No. 20CX9ZA060).

Institutional Review Board Statement: Not applicable.

Informed Consent Statement: Not applicable.

Data Availability Statement: The data presented in this study are available in the Supplementary Materials, or please contact the first author of this article.

Acknowledgments: Thanks are given to Pengfei Xue, Chenli Liu, Jing Ge, Mengjing Hou, Yuanchun Li, Jie Liu, Ruijing Wang, Xinyue Meng, Weiye Huang, Bin Liu, and Xuejing Shang from Lanzhou University, China, for their help in the field survey data collection. Specific thanks are given to the editors and four anonymous reviewers for their valuable suggestions and comments in the improvement of this work and manuscript.

Conflicts of Interest: The authors declare no conflict of interest.

References

1. Gong, P.; Wang, J.; Yu, L.; Zhao, Y.; Zhao, Y.; Liang, L.; Niu, Z.; Huang, X.; Fu, H.; Liu, S. Finer resolution observation and monitoring of global land cover: First mapping results with Landsat TM and ETM+ data. *Int. J. Remote Sens.* **2013**, *34*, 2607–2654. [CrossRef]
2. Lambin, E.F.; Meyfroidt, P. Global land use change, economic globalization, and the looming land scarcity. *Proc. Natl. Acad. Sci. USA* **2011**, *108*, 3465–3472. [CrossRef] [PubMed]
3. Turner, B.L.; Lambin, E.F.; Reenberg, A. The emergence of land change science for global environmental change and sustainability. *Proc. Natl. Acad. Sci. USA* **2007**, *104*, 20666–20671. [CrossRef]
4. Song, X.-P.; Hansen, M.C.; Stehman, S.V.; Potapov, P.V.; Tyukavina, A.; Vermote, E.F.; Townshend, J.R. Global land change from 1982 to 2016. *Nature* **2018**, *560*, 639–643. [CrossRef] [PubMed]
5. Foley, J.A.; DeFries, R.; Asner, G.P.; Barford, C.; Bonan, G.; Carpenter, S.R.; Chapin, F.S.; Coe, M.T.; Daily, G.C.; Gibbs, H.K. Global consequences of land use. *Science* **2005**, *309*, 570–574. [CrossRef]
6. Le Quéré, C.; Andrew, R.M.; Canadell, J.G.; Sitch, S.; Korsbakken, J.I.; Peters, G.P.; Manning, A.C.; Boden, T.A.; Tans, P.P.; Houghton, R.A. Global carbon budget 2016. *Earth Syst. Sci. Data* **2016**, *8*, 605–649. [CrossRef]
7. Gruber, N.; Galloway, J.N. An Earth-system perspective of the global nitrogen cycle. *Nature* **2008**, *451*, 293–296. [CrossRef]
8. Grimm, N.B.; Faeth, S.H.; Golubiewski, N.E.; Redman, C.L.; Wu, J.; Bai, X.; Briggs, J.M. Global change and the ecology of cities. *Science* **2008**, *319*, 756–760. [CrossRef]
9. Sterling, S.M.; Ducharne, A.; Polcher, J. The impact of global land-cover change on the terrestrial water cycle. *Nat. Clim. Change* **2013**, *3*, 385–390. [CrossRef]
10. Liu, X.; Liu, Y.; Wang, Y.; Liu, Z. Evaluating potential impacts of land use changes on water supply-demand under multiple development scenarios in dryland region. *J. Hydrol.* **2022**, *610*, 127811. [CrossRef]
11. Macedo, M.N.; DeFries, R.S.; Morton, D.C.; Stickler, C.M.; Galford, G.L.; Shimabukuro, Y.E. Decoupling of deforestation and soy production in the southern Amazon during the late 2000s. *Proc. Natl. Acad. Sci. USA* **2012**, *109*, 1341–1346. [CrossRef] [PubMed]
12. Morton, D.C.; DeFries, R.S.; Shimabukuro, Y.E.; Anderson, L.O.; Arai, E.; del Bon Espirito-Santo, F.; Freitas, R.; Morisette, J. Cropland expansion changes deforestation dynamics in the southern Brazilian Amazon. *Proc. Natl. Acad. Sci. USA* **2006**, *103*, 14637–14641. [CrossRef] [PubMed]
13. Xu, X.; Xie, Y.; Qi, K.; Luo, Z.; Wang, X. Detecting the response of bird communities and biodiversity to habitat loss and fragmentation due to urbanization. *Sci. Total Environ.* **2018**, *624*, 1561–1576. [CrossRef] [PubMed]
14. Llerena-Montoya, S.; Velastegui-Montoya, A.; Zhirzhan-Azanza, B.; Herrera-Matamoros, V.; Adami, M.; de Lima, A.; Moscoso-Silva, F.; Encalada, L. Multitemporal analysis of land use and land cover within an oil block in the Ecuadorian Amazon. *ISPRS Int. J. Geo-Inf.* **2021**, *10*, 191. [CrossRef]
15. Simmons, J.A.; Currie, W.S.; Eshleman, K.N.; Kuers, K.; Monteleone, S.; Negley, T.L.; Pohlad, B.R.; Thomas, C.L. Forest to reclaimed mine land use change leads to altered ecosystem structure and function. *Ecol. Appl.* **2008**, *18*, 104–118. [CrossRef] [PubMed]
16. Newbold, T.; Hudson, L.N.; Hill, S.L.; Contu, S.; Lysenko, I.; Senior, R.A.; Börger, L.; Bennett, D.J.; Choimes, A.; Collen, B. Global effects of land use on local terrestrial biodiversity. *Nature* **2015**, *520*, 45–50. [CrossRef] [PubMed]

17. Betts, M.G.; Wolf, C.; Ripple, W.J.; Phalan, B.; Millers, K.A.; Duarte, A.; Butchart, S.H.; Levi, T. Global forest loss disproportionately erodes biodiversity in intact landscapes. *Nature* **2017**, *547*, 441–444. [CrossRef] [PubMed]
18. Hou, M.; Bao, X.; Ge, J.; Liang, T. Land cover pattern and habitat suitability on the global largest breeding sites for Black-necked Cranes. *J. Clean. Prod.* **2021**, *322*, 128968. [CrossRef]
19. Nelson, E.; Sander, H.; Hawthorne, P.; Conte, M.; Ennaanay, D.; Wolny, S.; Manson, S.; Polasky, S. Projecting global land-use change and its effect on ecosystem service provision and biodiversity with simple models. *PLoS ONE* **2010**, *5*, e14327. [CrossRef] [PubMed]
20. Jones, K.R.; Venter, O.; Fuller, R.A.; Allan, J.R.; Maxwell, S.L.; Negret, P.J.; Watson, J.E. One-third of global protected land is under intense human pressure. *Science* **2018**, *360*, 788–791. [CrossRef]
21. Tassi, A.; Gigante, D.; Modica, G.; Di Martino, L.; Vizzari, M. Pixel-vs. Object-based landsat 8 data classification in google earth engine using random forest: The case study of maiella national park. *Remote Sens.* **2021**, *13*, 2299. [CrossRef]
22. Liu, C.; Li, W.; Zhu, G.; Zhou, H.; Yan, H.; Xue, P. Land use/land cover changes and their driving factors in the Northeastern Tibetan Plateau based on Geographical Detectors and Google Earth Engine: A case study in Gannan Prefecture. *Remote Sens.* **2020**, *12*, 3139. [CrossRef]
23. Xu, P.; Herold, M.; Tsendbazar, N.-E.; Clevers, J.G. Towards a comprehensive and consistent global aquatic land cover characterization framework addressing multiple user needs. *Remote Sens. Environ.* **2020**, *250*, 112034. [CrossRef]
24. Chen, J.; Chen, J.; Liao, A.; Cao, X.; Chen, L.; Chen, X.; He, C.; Han, G.; Peng, S.; Lu, M. Global land cover mapping at 30 m resolution: A POK-based operational approach. *ISPRS J. Photogramm. Remote Sens.* **2015**, *103*, 7–27. [CrossRef]
25. González-González, A.; Clerici, N.; Quesada, B. A 30 m-resolution land use-land cover product for the Colombian Andes and Amazon using cloud-computing. *Int. J. Appl. Earth Obs. Geoinf.* **2022**, *107*, 102688. [CrossRef]
26. Meng, B.; Zhang, Y.; Yang, Z.; Lv, Y.; Chen, J.; Li, M.; Sun, Y.; Zhang, H.; Yu, H.; Zhang, J. Mapping Grassland Classes Using Unmanned Aerial Vehicle and MODIS NDVI Data for Temperate Grassland in Inner Mongolia, China. *Remote Sens.* **2022**, *14*, 2094. [CrossRef]
27. Yao, J.; Wu, J.; Xiao, C.; Zhang, Z.; Li, J. The Classification Method Study of Crops Remote Sensing with Deep Learning, Machine Learning, and Google Earth Engine. *Remote Sens.* **2022**, *14*, 2758. [CrossRef]
28. Drusch, M.; Del Bello, U.; Carlier, S.; Colin, O.; Fernandez, V.; Gascon, F.; Hoersch, B.; Isola, C.; Laberinti, P.; Martimort, P. Sentinel-2: ESA's optical high-resolution mission for GMES operational services. *Remote Sens. Environ.* **2012**, *120*, 25–36. [CrossRef]
29. Huang, B.; Zhao, B.; Song, Y. Urban land-use mapping using a deep convolutional neural network with high spatial resolution multispectral remote sensing imagery. *Remote Sens. Environ.* **2018**, *214*, 73–86. [CrossRef]
30. Roy, D.P.; Wulder, M.A.; Loveland, T.R.; Woodcock, C.E.; Allen, R.G.; Anderson, M.C.; Helder, D.; Irons, J.R.; Johnson, D.M.; Kennedy, R. Landsat-8: Science and product vision for terrestrial global change research. *Remote Sens. Environ.* **2014**, *145*, 154–172. [CrossRef]
31. Chen, Y.; Lin, Z.; Zhao, X.; Wang, G.; Gu, Y. Deep learning-based classification of hyperspectral data. *IEEE J. Sel. Top. Appl. Earth Obs. Remote Sens.* **2014**, *7*, 2094–2107. [CrossRef]
32. Liu, Z.J.; Liu, Y.S.; Dong, J.W.; Baig, M.H.A.; Chi, W.F.; Peng, L.Y.; Wang, J.Y. Patterns and causes of winter wheat and summer maize rotation area change over the North China Plain. *Environ. Res. Lett.* **2022**, *17*, 044056. [CrossRef]
33. You, N.; Dong, J.; Huang, J.; Du, G.; Zhang, G.; He, Y.; Yang, T.; Di, Y.; Xiao, X. The 10-m crop type maps in Northeast China during 2017–2019. *Sci. Data* **2021**, *8*, 1–11. [CrossRef]
34. Wang, M.; Liu, Z.; Baig, M.H.A.; Wang, Y.; Li, Y.; Chen, Y. Mapping sugarcane in complex landscapes by integrating multi-temporal Sentinel-2 images and machine learning algorithms. *Land Use Policy* **2019**, *88*, 104190. [CrossRef]
35. Forkuor, G.; Dimobe, K.; Serme, I.; Tondoh, J.E. Landsat-8 vs. Sentinel-2: Examining the added value of sentinel-2′s red-edge bands to land-use and land-cover mapping in Burkina Faso. *Giscience Remote Sens.* **2018**, *55*, 331–354. [CrossRef]
36. Jin, Z.; Azzari, G.; You, C.; Di Tommaso, S.; Aston, S.; Burke, M.; Lobell, D.B. Smallholder maize area and yield mapping at national scales with Google Earth Engine. *Remote Sens. Environ.* **2019**, *228*, 115–128. [CrossRef]
37. Ma, Y.; Wu, H.; Wang, L.; Huang, B.; Ranjan, R.; Zomaya, A.; Jie, W. Remote sensing big data computing: Challenges and opportunities. *Future Gener. Comput. Syst.* **2015**, *51*, 47–60. [CrossRef]
38. Tamiminia, H.; Salehi, B.; Mahdianpari, M.; Quackenbush, L.; Adeli, S.; Brisco, B. Google Earth Engine for geo-big data applications: A meta-analysis and systematic review. *ISPRS J. Photogramm. Remote Sens.* **2020**, *164*, 152–170. [CrossRef]
39. Gorelick, N.; Hancher, M.; Dixon, M.; Ilyushchenko, S.; Thau, D.; Moore, R. Google Earth Engine: Planetary-scale geospatial analysis for everyone. *Remote Sens. Environ.* **2017**, *202*, 18–27. [CrossRef]
40. Xu, H.; Qi, S.; Li, X.; Gao, C.; Wei, Y.; Liu, C. Monitoring three-decade dynamics of citrus planting in Southeastern China using dense Landsat records. *Int. J. Appl. Earth Obs. Geoinf.* **2021**, *103*, 102518. [CrossRef]
41. Ge, J.; Meng, B.; Liang, T.; Feng, Q.; Gao, J.; Yang, S.; Huang, X.; Xie, H. Modeling alpine grassland cover based on MODIS data and support vector machine regression in the headwater region of the Huanghe River, China. *Remote Sens. Environ.* **2018**, *218*, 162–173. [CrossRef]
42. Ji, Q.; Liang, W.; Fu, B.; Zhang, W.; Yan, J.; Lü, Y.; Yue, C.; Jin, Z.; Lan, Z.; Li, S. Mapping land use/cover dynamics of the Yellow River Basin from 1986 to 2018 supported by Google Earth Engine. *Remote Sens.* **2021**, *13*, 1299. [CrossRef]

43. Hou, M.; Ge, J.; Gao, J.; Meng, B.; Li, Y.; Yin, J.; Liu, J.; Feng, Q.; Liang, T. Ecological risk assessment and impact factor analysis of alpine wetland ecosystem based on LUCC and boosted regression tree on the Zoige Plateau, China. *Remote Sens.* **2020**, *12*, 368. [CrossRef]
44. Wohlfart, C.; Liu, G.; Huang, C.; Kuenzer, C. A River Basin over the course of time: Multi-temporal analyses of land surface dynamics in the Yellow River Basin (China) based on medium resolution remote sensing data. *Remote Sens.* **2016**, *8*, 186. [CrossRef]
45. Wang, Y.; Huang, X.; Wang, J.; Zhou, M.; Liang, T. AMSR2 snow depth downscaling algorithm based on a multifactor approach over the Tibetan Plateau, China. *Remote Sens. Environ.* **2019**, *231*, 111268. [CrossRef]
46. Ye, C.; Sun, J.; Liu, M.; Xiong, J.; Zong, N.; Hu, J.; Huang, Y.; Duan, X.; Tsunekawa, A. Concurrent and lagged effects of extreme drought induce net reduction in vegetation carbon uptake on Tibetan Plateau. *Remote Sens.* **2020**, *12*, 2347. [CrossRef]
47. Bryan, B.A.; Gao, L.; Ye, Y.; Sun, X.; Connor, J.D.; Crossman, N.D.; Stafford-Smith, M.; Wu, J.; He, C.; Yu, D. China's response to a national land-system sustainability emergency. *Nature* **2018**, *559*, 193–204. [CrossRef]
48. Gong, P.; Liu, H.; Zhang, M.N.; Li, C.C.; Wang, J.; Huang, H.B.; Clinton, N.; Ji, L.Y.; Li, W.Y.; Bai, Y.Q.; et al. Stable classification with limited sample: Transferring a 30-m resolution sample set collected in 2015 to mapping 10-m resolution global land cover in 2017. *Sci. Bull.* **2019**, *64*, 370–373. [CrossRef]
49. Chen, Y.; Syvitski, J.P.; Gao, S.; Overeem, I.; Kettner, A.J. Socio-economic impacts on flooding: A 4000-year history of the Yellow River, China. *Ambio* **2012**, *41*, 682–698. [CrossRef]
50. Yang, Y.; Yang, D.; Wang, X.; Zhang, Z.; Nawaz, Z. Testing accuracy of land cover classification algorithms in the qilian mountains based on gee cloud platform. *Remote Sens.* **2021**, *13*, 5064. [CrossRef]
51. Gao, J.; Liang, T.; Liu, J.; Yin, J.; Ge, J.; Hou, M.; Feng, Q.; Wu, C.; Xie, H. Potential of hyperspectral data and machine learning algorithms to estimate the forage carbon-nitrogen ratio in an alpine grassland ecosystem of the Tibetan Plateau. *ISPRS J. Photogramm. Remote Sens.* **2020**, *163*, 362–374. [CrossRef]
52. Ma, Y.; Huang, X.; Feng, Q.; Liang, T. Alpine Grassland Reviving Response to Seasonal Snow Cover on the Tibetan Plateau. *Remote Sens.* **2022**, *14*, 2499. [CrossRef]
53. Chen, C.; Ma, Y.; Ren, G.; Wang, J. Aboveground biomass of salt-marsh vegetation in coastal wetlands: Sample expansion of in situ hyperspectral and Sentinel-2 data using a generative adversarial network. *Remote Sens. Environ.* **2022**, *270*, 112885. [CrossRef]
54. Zekoll, V.; Main-Knorn, M.; Alonso, K.; Louis, J.; Frantz, D.; Richter, R.; Pflug, B. Comparison of masking algorithms for sentinel-2 imagery. *Remote Sens.* **2021**, *13*, 137. [CrossRef]
55. Wang, Z.; Wu, B.; Zhang, M.; Zeng, H.; Yang, L.; Tian, F.; Ma, Z.; Wu, H. Indices enhance biological soil crust mapping in sandy and desert lands. *Remote Sens. Environ.* **2022**, *278*, 113078. [CrossRef]
56. Xi, Z.; Xu, H.; Xing, Y.; Gong, W.; Chen, G.; Yang, S. Forest Canopy Height Mapping by Synergizing ICESat-2, Sentinel-1, Sentinel-2 and Topographic Information Based on Machine Learning Methods. *Remote Sens.* **2022**, *14*, 364. [CrossRef]
57. Farr, T.G.; Rosen, P.A.; Caro, E.; Crippen, R.; Duren, R.; Hensley, S.; Kobrick, M.; Paller, M.; Rodriguez, E.; Roth, L. The shuttle radar topography mission. *Rev. Geophys.* **2007**, *45*. [CrossRef]
58. Meng, B.; Yang, Z.; Yu, H.; Qin, Y.; Sun, Y.; Zhang, J.; Chen, J.; Wang, Z.; Zhang, W.; Li, M.; et al. Mapping of Kobresia pygmaea Community Based on Umanned Aerial Vehicle Technology and Gaofen Remote Sensing Data in Alpine Meadow Grassland: A Case Study in Eastern of Qinghai–Tibetan Plateau. *Remote Sens.* **2021**, *13*, 2483. [CrossRef]
59. Huang, H.; Chen, Y.; Clinton, N.; Wang, J.; Wang, X.; Liu, C.; Gong, P.; Yang, J.; Bai, Y.; Zheng, Y. Mapping major land cover dynamics in Beijing using all Landsat images in Google Earth Engine. *Remote Sens. Environ.* **2017**, *202*, 166–176. [CrossRef]
60. Dubertret, F.; Le Tourneau, F.-M.; Villarreal, M.L.; Norman, L.M. Monitoring Annual Land Use/Land Cover Change in the Tucson Metropolitan Area with Google Earth Engine (1986–2020). *Remote Sens.* **2022**, *14*, 2127. [CrossRef]
61. Waśniewski, A.; Hościło, A.; Chmielewska, M. Can a Hierarchical Classification of Sentinel-2 Data Improve Land Cover Mapping? *Remote Sens.* **2022**, *14*, 989. [CrossRef]
62. Ouyang, Z.; Zhang, L.; Wu, B.; Li, X.; Xu, W.; Xiao, Y.; Zheng, H. An ecosystem classification system based on remote sensor information in China. *Acta Ecol. Sin.* **2015**, *35*, 219–226.
63. Loveland, T.R.; Reed, B.C.; Brown, J.F.; Ohlen, D.O.; Zhu, Z.; Yang, L.; Merchant, J.W. Development of a global land cover characteristics database and IGBP DISCover from 1 km AVHRR data. *Int. J. Remote Sens.* **2000**, *21*, 1303–1330. [CrossRef]
64. Congalton, R.G.; Gu, J.; Yadav, K.; Thenkabail, P.; Ozdogan, M. Global land cover mapping: A review and uncertainty analysis. *Remote Sens.* **2014**, *6*, 12070–12093. [CrossRef]
65. Roy, P.S.; Roy, A.; Joshi, P.K.; Kale, M.P.; Srivastava, V.K.; Srivastava, S.K.; Dwevidi, R.S.; Joshi, C.; Behera, M.D.; Meiyappan, P.; et al. Development of Decadal (1985–1995–2005) Land Use and Land Cover Database for India. *Remote Sens.* **2015**, *7*, 2401–2430. [CrossRef]
66. Vizzari, M. PlanetScope, Sentinel-2, and Sentinel-1 Data Integration for Object-Based Land Cover Classification in Google Earth Engine. *Remote Sens.* **2022**, *14*, 2628. [CrossRef]
67. Pott, L.P.; Amado, T.J.C.; Schwalbert, R.A.; Corassa, G.M.; Ciampitti, I.A. Satellite-based data fusion crop type classification and mapping in Rio Grande do Sul, Brazil. *ISPRS J. Photogramm. Remote Sens.* **2021**, *176*, 196–210. [CrossRef]
68. Verde, N.; Kokkoris, I.P.; Georgiadis, C.; Kaimaris, D.; Dimopoulos, P.; Mitsopoulos, I.; Mallinis, G. National scale land cover classification for ecosystem services mapping and assessment, using multitemporal copernicus EO data and google earth engine. *Remote Sens.* **2020**, *12*, 3303. [CrossRef]

69. Tuvdendorj, B.; Zeng, H.; Wu, B.; Elnashar, A.; Zhang, M.; Tian, F.; Nabil, M.; Nanzad, L.; Bulkhbai, A.; Natsagdorj, N. Performance and the Optimal Integration of Sentinel-1/2 Time-Series Features for Crop Classification in Northern Mongolia. *Remote Sens.* **2022**, *14*, 1830. [CrossRef]
70. Fremout, T.; Cobián-De Vinatea, J.; Thomas, E.; Huaman-Zambrano, W.; Salazar-Villegas, M.; Limache-de la Fuente, D.; Bernardino, P.N.; Atkinson, R.; Csaplovics, E.; Muys, B. Site-specific scaling of remote sensing-based estimates of woody cover and aboveground biomass for mapping long-term tropical dry forest degradation status. *Remote Sens. Environ.* **2022**, *276*, 113040. [CrossRef]
71. Amini, S.; Saber, M.; Rabiei-Dastjerdi, H.; Homayouni, S. Urban Land Use and Land Cover Change Analysis Using Random Forest Classification of Landsat Time Series. *Remote Sens.* **2022**, *14*, 2654. [CrossRef]
72. Tucker, C.J. Red and photographic infrared linear combinations for monitoring vegetation. *Remote Sens. Environ.* **1979**, *8*, 127–150. [CrossRef]
73. Gao, B.-C. NDWI—A normalized difference water index for remote sensing of vegetation liquid water from space. *Remote Sens. Environ.* **1996**, *58*, 257–266. [CrossRef]
74. Zha, Y.; Gao, J.; Ni, S. Use of normalized difference built-up index in automatically mapping urban areas from TM imagery. *Int. J. Remote Sens.* **2003**, *24*, 583–594. [CrossRef]
75. Huete, A.R. A soil-adjusted vegetation index (SAVI). *Remote Sens. Environ.* **1988**, *25*, 295–309. [CrossRef]
76. Huete, A.; Didan, K.; Miura, T.; Rodriguez, E.P.; Gao, X.; Ferreira, L.G. Overview of the radiometric and biophysical performance of the MODIS vegetation indices. *Remote Sens. Environ.* **2002**, *83*, 195–213. [CrossRef]
77. Johansen, K.; Phinn, S. Mapping structural parameters and species composition of riparian vegetation using IKONOS and Landsat ETM+ data in Australian tropical savannahs. *Photogramm. Eng. Remote Sens.* **2006**, *72*, 71–80. [CrossRef]
78. Fassnacht, F.E.; Latifi, H.; Stereńczak, K.; Modzelewska, A.; Lefsky, M.; Waser, L.T.; Straub, C.; Ghosh, A. Review of studies on tree species classification from remotely sensed data. *Remote Sens. Environ.* **2016**, *186*, 64–87. [CrossRef]
79. Mohammadpour, P.; Viegas, D.X.; Viegas, C. Vegetation Mapping with Random Forest Using Sentinel 2 and GLCM Texture Feature—A Case Study for Lousã Region, Portugal. *Remote Sens.* **2022**, *14*, 4585. [CrossRef]
80. Haralick, R.M.; Shanmugam, K.; Dinstein, I.H. Textural features for image classification. *IEEE Trans. Syst. Man Cybern.* **1973**, *SMC-3*, 610–621. [CrossRef]
81. Kupidura, P. The comparison of different methods of texture analysis for their efficacy for land use classification in satellite imagery. *Remote Sens.* **2019**, *11*, 1233. [CrossRef]
82. Tassi, A.; Vizzari, M. Object-oriented lulc classification in google earth engine combining snic, glcm, and machine learning algorithms. *Remote Sens.* **2020**, *12*, 3776. [CrossRef]
83. Zhang, X.; Zeraatpisheh, M.; Rahman, M.M.; Wang, S.; Xu, M. Texture is important in improving the accuracy of mapping photovoltaic power plants: A case study of Ningxia Autonomous Region, China. *Remote Sens.* **2021**, *13*, 3909. [CrossRef]
84. Breiman, L. Random forests. *Mach. Learn.* **2001**, *45*, 5–32. [CrossRef]
85. Pelletier, C.; Valero, S.; Inglada, J.; Champion, N.; Dedieu, G. Assessing the robustness of Random Forests to map land cover with high resolution satellite image time series over large areas. *Remote Sens. Environ.* **2016**, *187*, 156–168. [CrossRef]
86. Belgiu, M.; Drăguţ, L. Random forest in remote sensing: A review of applications and future directions. *ISPRS J. Photogramm. Remote Sens.* **2016**, *114*, 24–31. [CrossRef]
87. Hemmerling, J.; Pflugmacher, D.; Hostert, P. Mapping temperate forest tree species using dense Sentinel-2 time series. *Remote Sens. Environ.* **2021**, *267*, 112743. [CrossRef]
88. Wei, P.; Zhu, W.; Zhao, Y.; Fang, P.; Zhang, X.; Yan, N.; Zhao, H. Extraction of Kenyan Grassland Information Using PROBA-V Based on RFE-RF Algorithm. *Remote Sens.* **2021**, *13*, 4762. [CrossRef]
89. Rodriguez-Galiano, V.F.; Ghimire, B.; Rogan, J.; Chica-Olmo, M.; Rigol-Sanchez, J.P. An assessment of the effectiveness of a random forest classifier for land-cover classification. *ISPRS J. Photogramm. Remote Sens.* **2012**, *67*, 93–104. [CrossRef]
90. Talukdar, S.; Singha, P.; Mahato, S.; Pal, S.; Liou, Y.-A.; Rahman, A. Land-use land-cover classification by machine learning classifiers for satellite observations—A review. *Remote Sens.* **2020**, *12*, 1135. [CrossRef]
91. Li, W.; Dong, R.; Fu, H.; Wang, J.; Yu, L.; Gong, P. Integrating Google Earth imagery with Landsat data to improve 30-m resolution land cover mapping. *Remote Sens. Environ.* **2020**, *237*, 111563. [CrossRef]
92. Huang, W.; Li, W.; Xu, J.; Ma, X.; Li, C.; Liu, C. Hyperspectral Monitoring Driven by Machine Learning Methods for Grassland Above-Ground Biomass. *Remote Sens.* **2022**, *14*, 2086. [CrossRef]
93. Qi, S.; Song, B.; Liu, C.; Gong, P.; Luo, J.; Zhang, M.; Xiong, T. Bamboo Forest Mapping in China Using the Dense Landsat 8 Image Archive and Google Earth Engine. *Remote Sens.* **2022**, *14*, 762. [CrossRef]
94. Congalton, R.G. A review of assessing the accuracy of classifications of remotely sensed data. *Remote Sens. Environ.* **1991**, *37*, 35–46. [CrossRef]
95. Foody, G.M. Status of land cover classification accuracy assessment. *Remote Sens. Environ.* **2002**, *80*, 185–201. [CrossRef]
96. Rosenfield, G.H.; Fitzpatrick-Lins, K. A coefficient of agreement as a measure of thematic classification accuracy. *Photogramm. Eng. Remote Sens.* **1986**, *52*, 223–227.
97. Stehman, S.V. Selecting and interpreting measures of thematic classification accuracy. *Remote Sens. Environ.* **1997**, *62*, 77–89. [CrossRef]

98. Mostafa, E.; Li, X.; Sadek, M.; Dossou, J.F. Monitoring and Forecasting of Urban Expansion Using Machine Learning-Based Techniques and Remotely Sensed Data: A Case Study of Gharbia Governorate, Egypt. *Remote Sens.* **2021**, *13*, 4498. [CrossRef]
99. Olofsson, P.; Foody, G.M.; Herold, M.; Stehman, S.V.; Woodcock, C.E.; Wulder, M.A. Good practices for estimating area and assessing accuracy of land change. *Remote Sens. Environ.* **2014**, *148*, 42–57. [CrossRef]
100. Naboureh, A.; Li, A.; Ebrahimy, H.; Bian, J.; Azadbakht, M.; Amani, M.; Lei, G.; Nan, X. Assessing the effects of irrigated agricultural expansions on Lake Urmia using multi-decadal Landsat imagery and a sample migration technique within Google Earth Engine. *Int. J. Appl. Earth Obs. Geoinf.* **2021**, *105*, 102607. [CrossRef]
101. Tsujimoto, M.; Kajikawa, Y.; Tomita, J.; Matsumoto, Y. A review of the ecosystem concept—Towards coherent ecosystem design. *Technol. Forecast. Soc. Change* **2018**, *136*, 49–58. [CrossRef]
102. Tansley, A.G. The use and abuse of vegetational concepts and terms. *Ecology* **1935**, *16*, 284–307. [CrossRef]
103. Sparrow, B.D.; Edwards, W.; Munroe, S.E.; Wardle, G.M.; Guerin, G.R.; Bastin, J.F.; Morris, B.; Christensen, R.; Phinn, S.; Lowe, A.J. Effective ecosystem monitoring requires a multi-scaled approach. *Biol. Rev.* **2020**, *95*, 1706–1719. [CrossRef] [PubMed]
104. Vogelmann, J.E.; Xian, G.; Homer, C.; Tolk, B. Monitoring gradual ecosystem change using Landsat time series analyses: Case studies in selected forest and rangeland ecosystems. *Remote Sens. Environ.* **2012**, *122*, 92–105. [CrossRef]
105. Odum, E.P.; Barrett, G.W. *Fundamentals of Ecology*; Saunders: Philadelphia, PA, USA, 1971; Volume 3.
106. Luken, J.O. *Directing Ecological Succession*; Springer Science & Business Media: Berlin/Heidelberg, Germany, 1990.
107. Coradini, K.; Krejčová, J.; Frouz, J. Potential of vegetation and woodland cover recovery during primary and secondary succession, a global quantitative review. *Land Degrad. Dev.* **2022**, *33*, 512–526. [CrossRef]
108. Chang, C.C.; Turner, B.L. Ecological succession in a changing world. *J. Ecol.* **2019**, *107*, 503–509. [CrossRef]
109. Peltzer, D.A.; Wardle, D.A.; Allison, V.J.; Baisden, W.T.; Bardgett, R.D.; Chadwick, O.A.; Condron, L.M.; Parfitt, R.L.; Porder, S.; Richardson, S.J. Understanding ecosystem retrogression. *Ecol. Monogr.* **2010**, *80*, 509–529. [CrossRef]
110. Yan, J.; Zhang, Y.; Bai, W.; Liu, Y.; Bao, W.; Liu, L.; Zheng, D. Land cover changes based on plant successions: Deforestation, rehabilitation and degeneration of forest in the upper Dadu River watershed. *Sci. China Ser. D Earth Sci.* **2005**, *48*, 2214–2230. [CrossRef]
111. Bergen, K.M.; Dronova, I. Observing succession on aspen-dominated landscapes using a remote sensing-ecosystem approach. *Landsc. Ecol.* **2007**, *22*, 1395–1410. [CrossRef]
112. Temesgen, H.; Nyssen, J.; Zenebe, A.; Haregeweyn, N.; Kindu, M.; Lemenih, M.; Haile, M. Ecological succession and land use changes in a lake retreat area (Main Ethiopian Rift Valley). *J. Arid. Environ.* **2013**, *91*, 53–60. [CrossRef]
113. Friedman, J.H. Greedy function approximation: A gradient boosting machine. *Ann. Stat.* **2001**, *29*, 1189–1232. [CrossRef]
114. De'ath, G.; Fabricius, K.E. Classification and regression trees: A powerful yet simple technique for ecological data analysis. *Ecology* **2000**, *81*, 3178–3192. [CrossRef]
115. Cortes, C.; Vapnik, V. Support-vector networks. *Mach. Learn.* **1995**, *20*, 273–297. [CrossRef]
116. Chen, Z.; Kang, Y.; Sun, Z.; Wu, F.; Zhang, Q. Extraction of Photovoltaic Plants Using Machine Learning Methods: A Case Study of the Pilot Energy City of Golmud, China. *Remote Sens.* **2022**, *14*, 2697. [CrossRef]
117. Burai, P.; Deák, B.; Valkó, O.; Tomor, T. Classification of Herbaceous Vegetation Using Airborne Hyperspectral Imagery. *Remote Sens.* **2015**, *7*, 2046–2066. [CrossRef]
118. Ghayour, L.; Neshat, A.; Paryani, S.; Shahabi, H.; Shirzadi, A.; Chen, W.; Al-Ansari, N.; Geertsema, M.; Pourmehdi Amiri, M.; Gholamnia, M.; et al. Performance Evaluation of Sentinel-2 and Landsat 8 OLI Data for Land Cover/Use Classification Using a Comparison between Machine Learning Algorithms. *Remote Sens.* **2021**, *13*, 1349. [CrossRef]
119. Saboori, M.; Homayouni, S.; Shah-Hosseini, R.; Zhang, Y. Optimum Feature and Classifier Selection for Accurate Urban Land Use/Cover Mapping from Very High Resolution Satellite Imagery. *Remote Sens.* **2022**, *14*, 2097. [CrossRef]
120. Rapinel, S.; Mony, C.; Lecoq, L.; Clement, B.; Thomas, A.; Hubert-Moy, L. Evaluation of Sentinel-2 time-series for mapping floodplain grassland plant communities. *Remote Sens. Environ.* **2019**, *223*, 115–129. [CrossRef]
121. Xiong, K.; Adhikari, B.R.; Stamatopoulos, C.A.; Zhan, Y.; Wu, S.; Dong, Z.; Di, B. Comparison of Different Machine Learning Methods for Debris Flow Susceptibility Mapping: A Case Study in the Sichuan Province, China. *Remote Sens.* **2020**, *12*, 295. [CrossRef]
122. Liu, S.; Qi, Z.; Li, X.; Yeh, A.G.-O. Integration of convolutional neural networks and object-based post-classification refinement for land use and land cover mapping with optical and SAR data. *Remote Sens.* **2019**, *11*, 690. [CrossRef]
123. Holl, K.D.; Aide, T.M. When and where to actively restore ecosystems? *For. Ecol. Manag.* **2011**, *261*, 1558–1563. [CrossRef]
124. Ouyang, Z.; Zheng, H.; Xiao, Y.; Polasky, S.; Liu, J.; Xu, W.; Wang, Q.; Zhang, L.; Xiao, Y.; Rao, E. Improvements in ecosystem services from investments in natural capital. *Science* **2016**, *352*, 1455–1459. [CrossRef] [PubMed]
125. Li, W.; Wang, W.; Chen, J.; Zhang, Z. Assessing effects of the Returning Farmland to Forest Program on vegetation cover changes at multiple spatial scales: The case of northwest Yunnan, China. *J. Environ. Manag.* **2022**, *304*, 114303. [CrossRef] [PubMed]
126. Calderón-Loor, M.; Hadjikakou, M.; Bryan, B.A. High-resolution wall-to-wall land-cover mapping and land change assessment for Australia from 1985 to 2015. *Remote Sens. Environ.* **2021**, *252*, 112148. [CrossRef]
127. Li, W.; Xue, P.; Liu, C.; Yan, H.; Zhu, G.; Cao, Y. Monitoring and Landscape Dynamic Analysis of Alpine Wetland Area Based on Multiple Algorithms: A Case Study of Zoige Plateau. *Sensors* **2020**, *20*, 7315. [CrossRef]
128. You, N.; Dong, J. Examining earliest identifiable timing of crops using all available Sentinel 1/2 imagery and Google Earth Engine. *ISPRS J. Photogramm. Remote Sens.* **2020**, *161*, 109–123. [CrossRef]